

Attribution-NonCommercial-NoDerivatives 4.0 International (CC BY-NC-ND 4.0)

<https://creativecommons.org/licenses/by-nc-nd/4.0/>

<https://doi.org/10.1016/j.jqsrt.2022.108341>

Access to this work was provided by the University of Maryland, Baltimore County (UMBC) ScholarWorks@UMBC digital repository on the Maryland Shared Open Access (MD-SOAR) platform.

**Please provide feedback**

Please support the ScholarWorks@UMBC repository by emailing [scholarworks-group@umbc.edu](mailto:scholarworks-group@umbc.edu) and telling us what having access to this work means to you and why it's important to you. Thank you.

# VLIDORT-QS: A quasi-spherical vector radiative transfer model

R. Spurr<sup>(1)†</sup>, V. Natraj<sup>(2)</sup>, S. F. Colosimo<sup>(3)</sup>, J. Stutz<sup>(3)</sup>, M. Christi<sup>(4)</sup> and S. Korkin<sup>(5)</sup>

(1) RT SOLUTIONS Inc., Cambridge MA 02138.

(2) Jet Propulsion Laboratory, California Institute of Technology, Pasadena, CA 91109

(3) Department of Atmospheric and Oceanic Sciences, UCLA, Los Angeles, CA

(4) Fort Collins, CO

(5) University of Maryland, Baltimore County (UMBC), Baltimore, MD

Submitted to JQSRT, April 2022.

## Abstract

We present a new VLIDORT-based quasi-spherical vector radiative transfer (RT) model (VLIDORT-QS) that was developed for forward-model simulations of long-path measurements in limb- or nadir-viewing spherical-atmosphere configurations. This paper provides a theoretical description of the RT model, in which the single-scatter radiation field is treated accurately in spherical geometry, while the diffuse scatter source terms at points along the line-of-sight are approximated locally through pseudo-spherical simulations based on the VLIDORT RT code; these multiple scatter source terms are then folded into the source function integration to yield the radiation field at any line-of-sight observation point in the atmosphere. In addition, the VLIDORT-QS model has a complete linearization facility (ability to generate analytic Jacobians of the radiation field with respect to any atmospheric or surface property). Validation of the model has been carried out against a fully-spherical Monte Carlo code, and also against the standard VLIDORT model for nadir-view scenarios with relatively low sphericity effects. A sample application of VLIDORT-QS for a biomass-burning plume scenario is demonstrated. A second paper will present a detailed analysis of the retrieval of ice-cloud properties from high-altitude aircraft measurements taken as part of the NASA Airborne Tropical Tropopause Experiment (ATTREX) campaign, with VLIDORT-QS providing forward-model simulations of the radiation fields and associated Jacobian functions.

†Corresponding Author. Email: rtsolutions@verizon.net

# 1. Introduction

There is a whole range of fully-spherical and approximately-spherical radiative transfer (RT) models available for light scattering studies in planetary atmospheres. A full 3-D spherical treatment for multiple scattering has so far only been done with Monte Carlo (MC) methods. The earliest set of spherical-atmosphere MC benchmark results was provided by [1]. Other MC models for Earth atmosphere studies include the MC++ [2], McArtim [3] and MYSTIC [4,5] codes.

Many approximately-spherical RT models are based on attempts to correct for sphericity effects in 1-D plane-parallel RT codes. There are a variety of approaches here, depending on the choice of RT solver. For example, several plane-parallel discrete-ordinate codes have been adapted to allow for sphericity; these include the DISORT code [6,7], the SCIATRAN model [8], the matrix-exponential model [9] and the LIDORT/VLIDORT codes [10,11]. Other approaches to RT sphericity have used the Gauss-Seidel approximation [12,13], the Picard iteration method [14,15], and the method of characteristics [16], to name just three examples. Many other variations could be mentioned here; for a recent comprehensive review of spherical RT codes of all types, see [17]. In the present work, our starting point is the VLIDORT model [11,18].

The expression “pseudo-spherical” is a rather broad term applied to several approaches to correct for spherical geometry effects. To avoid confusion, we use the phrase “regular pseudo-spherical (RPS)” to refer to a sphericity correction in which all incident solar beam attenuations are calculated for a curved atmosphere, with both single and multiple scattering still treated in a multi-layer plane-parallel medium. The RPS approximation has been a standard feature for a number of years now in many non-limb 1-D plane-parallel RT codes. A further sphericity correction to these codes involves the separate calculation of the single scatter (SS) radiation field in an accurate fully spherical configuration, by treating both incident and line-of-sight (LOS) paths for spherical curvature. This we will term the “enhanced pseudo-spherical (EPS)” approximation; the multiple scattering (MS) field is still treated in the RPS approach. The EPS correction is important for wide off-nadir viewing scenarios from remote-sensing satellites [10,19,20]. Both the RPS and EPS options are available in the LIDORT and VLIDORT models.

The EPS approximation allows SS layer source terms to follow changes in line-of-sight (LOS) path geometry. A logical next step towards accounting for spherical geometry is to also enable MS layer source terms to reflect LOS path geometry changes. These MS layer source terms are still calculated with the RPS approximation in a plane-parallel 1-D code, which is now called repeatedly along the LOS as the path geometry changes. This idea was first taken up for the LIDORT model several years ago [21], and is now a feature of the next release of the VLIDORT and LIDORT codes.

As an example, we consider satellite simulations of upwelling radiation at the top of the atmosphere (TOA), along a LOS from the bottom of the atmosphere (BOA). In the EPS approximation, a single call to VLIDORT for the BOA geometrical configuration (solar and viewing zenith angles, relative azimuth angle) will produce an accurate fully-spherical SS result, plus a diffuse MS field characterized by a set of MS layer source terms  $\{\mathbf{M}_n^{(BOA)}\}$  ( $n$  is a layer index). In order to allow for MS layer source term variations along the LOS, the easiest approach is to modify the call to VLIDORT to produce two sets of MS layer source terms  $\{\mathbf{M}_n^{(BOA)}\}$  and  $\{\mathbf{M}_n^{(TOA)}\}$  corresponding to two geometrical configurations at BOA and TOA, and then interpolate (with respect to the cosine of the LOS zenith angle) these MS layer source terms to values  $\{\mathbf{M}_n^{(LOS)}\}$  at other LOS geometrical configurations. This simple “2-point MS sphericity correction” is described in more detail in [17], where it was shown to be a very effective accuracy improvement (over

standard VLIDORT) when compared with fully-spherical MC output. Multi-point MS sphericity calculations using VLIDORT output are clearly possible; this would involve a single call to VLIDORT to deliver a collection of MS source terms for geometrical configurations at all layer boundaries along the LOS. We discuss these nadir-view sphericity corrections in Section 3.1 for validation of VLIDORT-QS against VLIDORT.

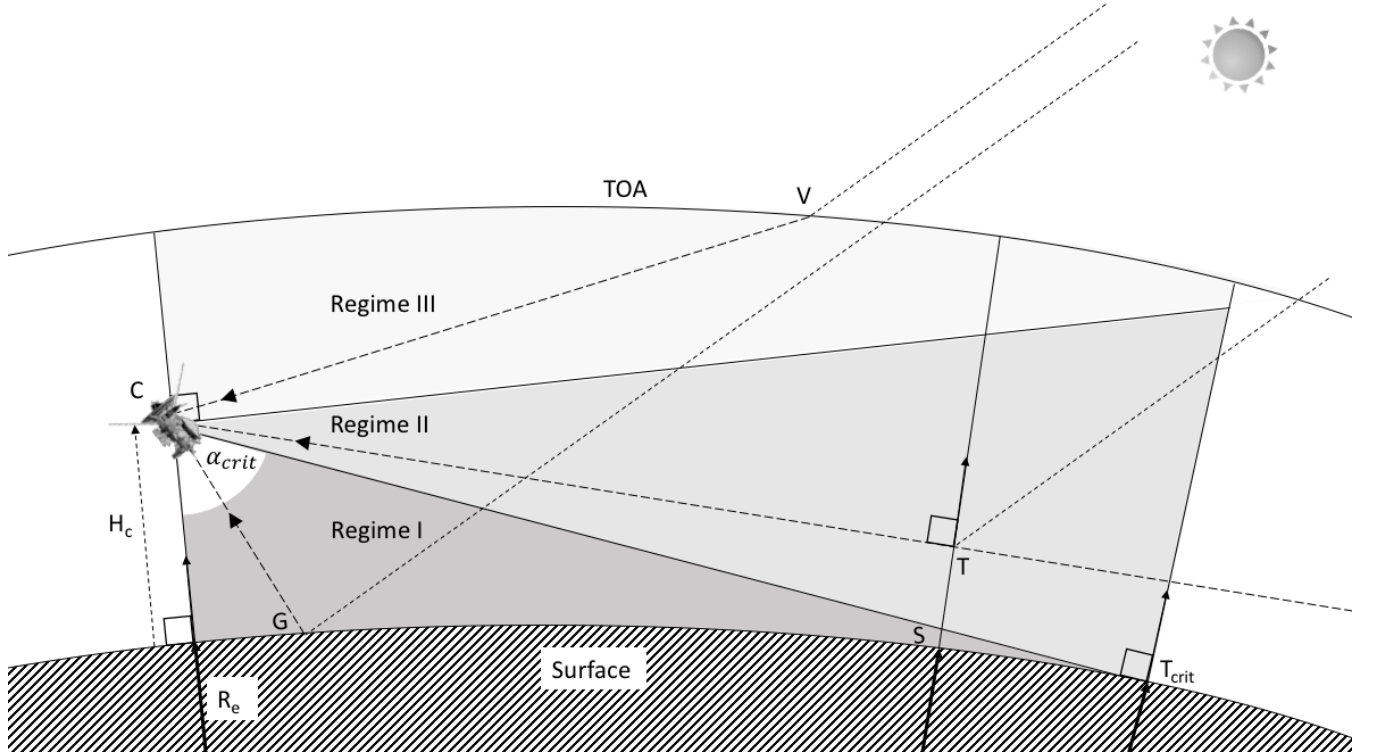


**Figure 1:** Viewing regimes for VLIDORT-QS (sketch is not to scale). Solar paths (parallel dotted lines) and line-of-sight (LOS) paths (dashed lines) are shown in the principal plane. Downwelling LOS paths in Regime III start from the top of the atmosphere (TOA) and finish at the camera position C (path V-C). Regime II represents the limb view scenario, where LOS paths originate at TOA, at the far right of tangent point T, passing through the tangent height on the way to C. Tangent height is defined as the distance from the surface to the tangent point T (path S-T). Upwelling LOS paths to C in Regime I originate at the surface (path G-C). The transition from Regime I to Regime II occurs when the tangent height touches the surface ( $T_{crit}$  in the figure), with critical angle  $\alpha_{crit} = \arcsin[R_e/(R_e + H_c)]$ , where  $H_c$  is the camera height and  $R_e$  the Earth's radius.

These sphericity corrections apply only to upwelling or downwelling nadir view scenarios. For LOS-path limb view situations, something more accurate is needed when dealing with MS layer terms, and VLIDORT-QS has been designed from the outset to deal with limb geometry. Referring to the sketch in Figure 1, there are three viewing regimes (the camera position is denoted by the letter C). These are:

1. (Regime I). The camera is looking down so that the LOS originates at the ground. This is the standard "nadir-upwelling" scenario typified by path CG originating at the ground. Light sources

include both direct-bounce and MS surface reflectance terms, in addition to single and multiple scattering in the atmosphere.

2. (Regime II). The camera is still looking downwards, but now the LOS passes through the atmosphere with no surface intersection. This is the "limb-view" scenario, with the LOS path passing through a tangent point T; this path starts at the top of the atmosphere on the far side of T, moving downwards through the atmosphere to T, then finishing in an upwelling direction on the near side of T towards the camera position C.
3. (Regime III). The camera is looking up, with the LOS starting directly at TOA (path VC). This is the standard "nadir-downwelling" scenario.

The LOS angle convention is to measure the viewing path zenith angle ( $\alpha$ ) relative to the upward looking nadir through the camera. The change from Regime I to Regime II occurs at a critical view angle at which the limb path is tangential to the surface. In terms of the view angle  $\alpha$  at the camera, we have  $0 \leq \alpha < \alpha_{crit}$  for Regime I,  $\alpha_{crit} \leq \alpha \leq \frac{\pi}{2}$  (Regime II) and  $\frac{\pi}{2} < \alpha < \pi$  for Regime III. Thus, if the radius of the Earth is  $R_e$  and the aircraft (camera) height is  $H_c$ ,  $\alpha_{crit} = \arcsin[R_e/(R_e + H_c)]$ . For  $H_c = 20$  km and  $R_e = 6371$  km,  $\alpha_{crit} = 85.466^\circ$ .

In a spherical-shell stratified atmosphere, LOS path segments are mostly defined by layer boundaries, but for Regime II limb viewing, partial-layer segments are needed on both sides of the tangent point. If the camera is situated between adjacent layer boundaries, then the final segment of the LOS will also pass through a partial layer. For an atmosphere with a 1-km height stratification, tangent-height path segments can be close to 113 km in length.

In VLIDORT-QS, the SS and MS contributions are calculated separately, with the SS model performing an accurate calculation in a curved-shell atmosphere, for all Regimes. The VLIDORT-QS MS calculations are based on the above-mentioned idea of allowing MS layer source terms to follow path geometry. MS scattering for each path segment is still treated using standard "RPS" VLIDORT, but VLIDORT-QS uses a more accurate approach to MS source term evaluation, without the use of interpolation. Instead, in each path segment, light scattered into the segment path is integrated numerically using a quadrature scheme based on a set of intermediate fine-level geometrical configurations along the segment path. For the MS part, we will use an adapted form of the VLIDORT RT model; *essentially, we take MS solutions to the RT equation (RTE) to be plane-parallel at all locations, but the post-processing (source function optical-thickness integration along the LOS) is done in full spherical geometry*. This is equivalent to a piecewise concatenation of 1-D MS RT solutions in a 3-D geometrical configuration. VLIDORT-QS is not a truly spherical model; it cannot deal with Earth-shadow scenarios and is confined to geometrical configurations in which all points on the LOS path are fully illuminated (that is, there are no incident-beam twilight situations, and solar zenith angles at all points along the path must be less than  $90^\circ$ ). The VLIDORT-QS model as presented here assumes a spherical-shell atmosphere of optically uniform sub-layers; horizontal variation of optical properties is not considered.

The first version of the VLIDORT-QS model was developed in May 2012 as part of an attempt to model observations from the Huygens probe taken during entry into the atmosphere of Saturn's moon Titan [22]. The VLIDORT-QS model was then adapted for the NASA Airborne Tropical Tropopause Experiment (ATTREX) project, which is concerned with limb- and nadir-scanning observations with a near-infrared (900–1726 nm) spectrometer on board NASA's high-altitude Global Hawk aircraft during the ATTREX mission [23]. A key motivation for ATTREX is the spectroscopic retrieval of path-averaged ice water absorption in cirrus clouds encountered during the ATTREX flights.

VLIDORT-QS is a vector model, dealing with polarized light fields. For all scenarios, it is necessary to give proper consideration to surface reflectance (many ATTREX mission flights were over the ocean), so the model was given a full bidirectional reflectance distribution function (BRDF) treatment of surface reflectance. With the need for optical property retrievals from ATTREX measurements, VLIDORT-QS was also given a linearization capability from the outset; the radiative transfer formulation is analytically differentiable with respect to any atmospheric or surface optical property. Jacobian derivations follow closely the linearization techniques used in the LIDORT and VLIDORT models (see [Spurr and Christi, 2019] for a recent review).

The paper has two main parts. In Section 2, we present a detailed description of the model, with three subsections dealing with the general RT formulation and the derivation of SS solutions (2.1), the treatment of MS source terms (2.2), and a discussion of the linearization facility (2.3). Section 3 is concerned with VLIDORT-QS validation, not only against the standard VLIDORT model with and without sphericity corrections (Section 3.1), but also through comparisons with spherical Monte Carlo RT output (Section 3.2). Section 4 contains a description of a biomass-burning application, showing how VLIDORT-QS can model the radiation field for a wide range of viewing paths both interior to and outside the smoke plume. Concluding remarks are in Section 5.

## 2. Description of the Model

### 2.1. Basic RT scenario and SS model

The basic geometrical input is a triplet of three angles at the camera position: the LOS zenith angle (LZA), the solar zenith angle (SZA), and the relative azimuth angle between the LOS and solar planes at this position (see Figure 2). Ray-tracing is necessary to compute all angle triplets at every layer boundary crossed by the LOS path (and at the tangent point for the limb-view Regime II configuration), and at every set of intermediate fine-levels as required by the source function integration.

The convention in VLIDORT-QS is to number the segments from the start of the path to the end at the camera position. Thus for pure downwelling (Regime III), the segment index  $s$  increases with the layer index  $n$ . For regime I, the segment index increases from the surface upwards, but the layer index  $n$  is decreasing. For Regime II, the path on the far side of the tangent point has indices  $s$  and  $n$  both increasing, then on the near side,  $s$  continues to increase but  $n$  is now decreasing.

We consider a single segment  $s$ , with Stokes vectors  $\mathbf{I}_s$  and  $\mathbf{I}_{s-1}$  for the radiation fields at the end and start of the segment, respectively. The corresponding geometries are  $G_s$  and  $G_{s-1}$ , where  $G_s = \{\alpha_s, \theta_s, \varphi_s\}$  is the triplet of angles (the LZA  $\alpha_s$ , the SZA  $\theta_s$  and the relative azimuth angle  $\varphi_s$ ). We assume straight-line geometry (no refraction), so that each path is characterized by a unique scattering angle  $\Theta$ :

$$\cos \Theta = \mp \cos \alpha_s \cos \theta_s + \sin \alpha_s \sin \theta_s \cos \varphi_s. \quad (2.1)$$

This angle is the same for all points on the path, with the  $\mp$  sign depending on the local up-or-down orientation of  $\alpha_s$ .

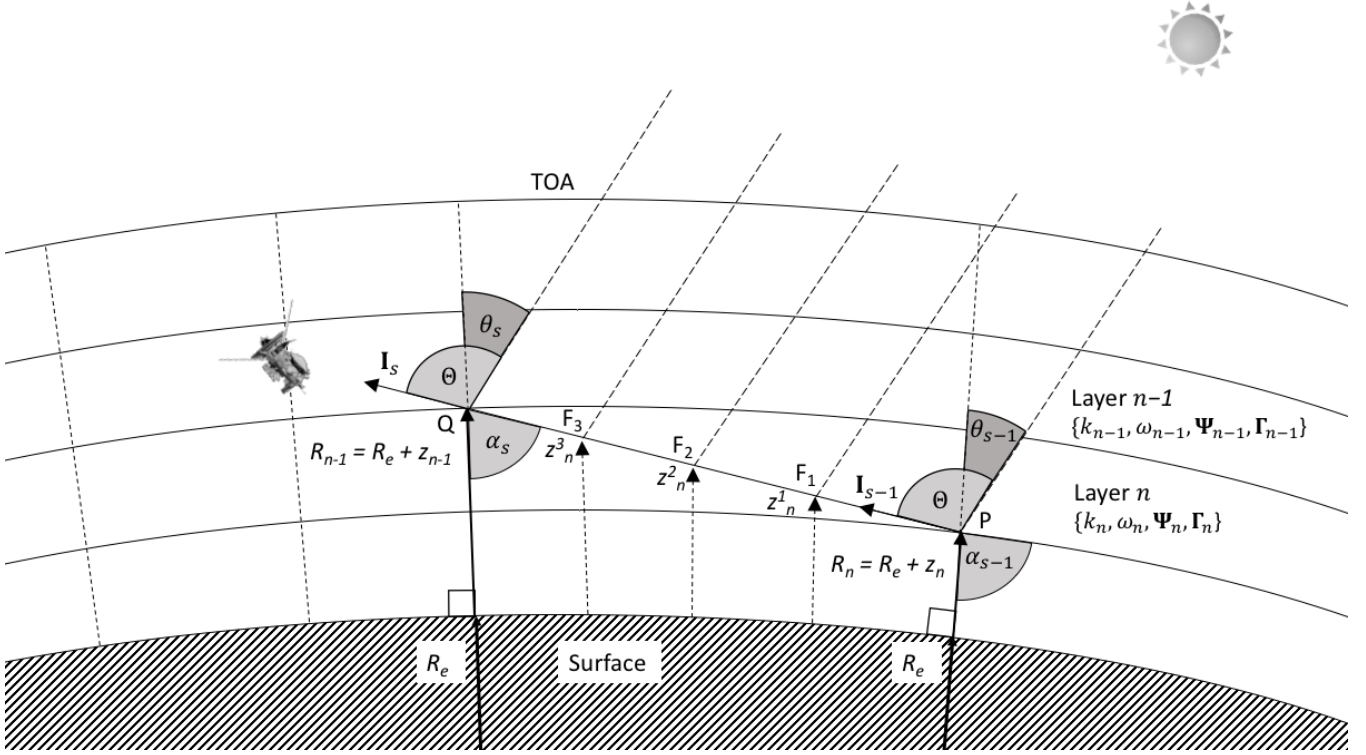


**Figure 2:** The LOS path makes passage from point P to point Q through layer  $n$  in a stratified atmosphere, corresponding to segment  $s$  (sketch is not to scale). The LZAs are  $\alpha_{s-1}$  at P, and  $\alpha_s$  at Q, with radii  $R_n$  and  $R_{n-1}$  respectively. SS of sunlight depends on the scattering angle  $\Theta$ , constant for a non-refractive atmosphere. Optical depth RTE integration along the LOS is done using a Gaussian quadrature scheme defined by the LOS angle range  $[\alpha_s, \alpha_{s-1}]$ , which allocates (inside the same layer  $n$ ) fine-layer points  $F_1$ ,  $F_2$ , and  $F_3$ , at heights corresponding to vertical coordinate  $z_n^1$ ,  $z_n^2$ , and  $z_n^3$ , respectively. Accurate solar-beam ray-tracing is performed using spherical geometry for these fine-layer divisions.

Each segment is uniquely associated with a layer  $n$  in a vertically stratified atmosphere, for which we assume a set of inherent optical properties (IOPs)  $\{k_n, \omega_n, \mathbf{\Gamma}_n\}$ ,  $n = 1, \dots, N_L$ . Here,  $N_L$  is the total number of layers, with  $k_n$  the layer extinction coefficient,  $\omega_n$  the layer single scattering albedo, and  $\mathbf{\Gamma}_n$  a  $4 \times 4$  matrix of spherical-function expansion coefficients for the layer. These IOPs represent total quantities (total extinction includes gas and particulate matter absorption, plus scatter-weighted molecular and particulate scattering); they are assumed constant for each layer. For a discussion on the creation and deployment of these properties, refer to the (V)LIDORT papers, for example [11].

For this segment corresponding to layer  $n$ , the RTE is written in terms of the vertical coordinate  $z$ :

$$\mu(z) \frac{d\mathbf{I}(z)}{dz} = -k_n \mathbf{I}(z) + k_n \omega_n \mathbf{H}_n(z). \quad (2.2)$$

Here, the cosine  $\mu(z) = \cos \alpha(z)$  is not a constant across the segment. Source term  $\mathbf{H}_n(z)$  at position  $z$  in the layer comprises two parts – the primary source function corresponding to SS of the solar beam, and a diffuse source function comprising an integration of the radiation field over all geometrical space.

In this section, we consider the SS solution, ignoring the diffuse contribution that is dealt with in the next section. For the SS solution,  $\mathbf{H}_n(z)$  depends on the scattering matrix  $\mathbf{\Psi}_n(z)$ , the local geometry  $G(z)$ , and the solar beam attenuation  $A_n(z)$ . The scattering matrix  $\mathbf{\Psi}_n(z)$  is developed through the use of generalized

spherical functions and the associated matrices of expansion coefficients  $\mathbf{\Gamma}_n$ . Indeed, we have the following:

$$\mathbf{H}_n(z) = \frac{F_*}{4\pi} A_n(z) \mathbf{\Psi}_n(z); \quad A_n(z) = \exp \left[ - \sum_{p=1}^{P(n)} d_{np}(z) k_p \right]. \quad (2.3)$$

The natural-light solar flux vector is  $\mathbf{F}_* = [F_*, 0, 0, 0]^T$ . In the expression for the attenuation  $A_n(z)$ , the beam will traverse a series of layers  $p = 1, \dots, P(n)$  on its way to the point of scatter in layer  $n$  at which the local height is  $z$ . Layer traverse distances  $d_{np}(z)$  will depend on the local solar angle at the point of scatter, and will be determined accurately through ray-tracing backwards along the LOS from the point of scatter to the camera. We do not consider solar illumination from below (no twilight or shadow configurations), so that the SZA is always less than  $90^\circ$  at every point along the path.

Since the LOS path is defined by the equation  $(R_e + z) \sin \alpha(z) = C$  for straight-line geometry with no refraction ( $C$  is the path constant), we change variable from  $z$  to  $\alpha(z)$ , and obtain an integrating factor for solving Eq. (2.2) with the source term in Eq. (2.3). Integrating from the start to the end of the segment, we then find that, for the upwelling case:

$$\mathbf{I}_s^\uparrow = T_s \mathbf{I}_{s-1}^\uparrow + \mathbf{L}_s^\uparrow; \quad (2.4)$$

$$\mathbf{L}_s^\uparrow = \omega_n \int_{\alpha_{s-1}}^{\alpha_s} \frac{\exp[-Ck_n(\cot \alpha - \cot \alpha_{s-1})] \mathbf{H}_n(\alpha)}{\sin^2 \alpha} d\alpha; \quad (2.5)$$

$$T_s = \exp[-Ck_n(\cot \alpha_s - \cot \alpha_{s-1})]. \quad (2.6)$$

Here,  $T_s$  is the segment attenuation (transmittance) along the LOS. A similar equation can be written down for any downwelling segment. The integrand in Eq. (2.5) is in general smoothly varying, and the integral itself is evaluated using Gauss-Legendre quadrature with abscissa and weights  $\{\alpha_j, \chi_j\}$  defined over the interval  $[\alpha_{s-1}, \alpha_s]$ . Using this, the SS layer source term  $\mathbf{L}_s^\uparrow$  may be written:

$$\mathbf{L}_s^\uparrow = \sum_{j=1}^{N_j} f_n(\alpha_j) \mathbf{H}_n(\alpha_j); \quad (2.7)$$

$$f_n(\alpha_j) = \omega_n \chi_j \frac{\exp[-Ck_n(\cot \alpha_j - \cot \alpha_{s-1})]}{\sin^2 \alpha_j}. \quad (2.8)$$

The number of weights  $N_j$  required will depend on how quickly the transmittance changes along the LOS for a given segment; we have found that  $N_j = 5$  is sufficient for most segments, with the exception of long-path Regime II segments adjacent to limb tangent heights (here,  $N_j = 8$  is the best choice). In summary, the main effort lies in the evaluation of  $\mathbf{H}_n(\alpha_j)$  at a series of quadrature points; this requires only the additional evaluation of solar beam attenuations  $A_n(\alpha_j)$  at these points.

Eqs. (2.4) to (2.8) comprise our basic formulation for the (upwelling) SS RT field. For limb-viewing scenarios, we will require both upwelling and downwelling segment evaluations. The SS model is completed when we apply Eq. (2.4) recursively to get the Stokes vector  $\mathbf{I}_{cam}$  at the camera:

$$\mathbf{I}_{cam} = \sum_{s=1}^{N_s} C_{s-1} \mathbf{L}_s; \quad C_{s>0} = \prod_{k=1}^s T_k; \quad C_0 = 1. \quad (\text{Regimes II and III}) \quad (2.9)$$



Here,  $\{C_s\}, s = 1, \dots, N_s$  are the *cumulative* LOS transmittances, where  $N_s$  is the total number of segments traversed. For Regime III, sources will only be downwelling, whereas for the limb-view in Regime II, sources will be downwelling for path segments on the far side of the tangent point, then upwelling for segments on the near side to the camera.

The above considerations apply to SS calculations in Regimes II and III, where there is no intersection with the surface. For Regime I, there is an additional “direct-bounce” (DB) contribution from surface reflection. For a Lambertian surface with albedo  $R$ , this contribution to  $\mathbf{I}_{N_s}$  is:

$$\mathbf{I}_{N_s}^{(DB)} = C_{N_s} \mathbf{I}_{Surf}^{(DB)}, \quad \mathbf{I}_{Surf}^{(DB)} = F_* \frac{R\mu_0}{\pi} A_{surf}(\mu_0). \quad (2.10)$$

For non-Lambertian surfaces, an equivalent expression for  $\mathbf{I}_{Surf}^{(DB)}$  can be found in terms of a suitable surface reflectance matrix. In Eq. (2.10),  $A_{surf}(\mu_0)$  is the solar beam attenuation to the bottom surface of the atmosphere (where the SZA cosine is  $\mu_0$ ). Thus, the final Regime I result is given by:

$$\mathbf{I}_{cam} = \mathbf{I}_{N_s}^{(DB)} + \sum_{s=1}^{N_s} C_{s-1} \mathbf{L}_s^\uparrow = C_{N_s} \mathbf{I}_{Surf}^{(DB)} + \sum_{s=1}^{N_s} C_{s-1} \mathbf{L}_s^\uparrow. \quad (\text{Regime I}). \quad (2.11)$$

## 2.2. MS source terms using VLIDORT

We now determine MS contributions using a specially adapted form of VLIDORT. In terms of the optical thickness coordinate  $x = k_n(z_{n-1} - z)$  (as measured from the top of layer  $n$  where the vertical height is  $z_{n-1}$ ), the full RTE in the VLIDORT model can be written as:

$$\mu \frac{d\mathbf{I}(x)}{dx} = -\mathbf{I}(x) + \omega_n \mathbf{H}_n(x); \quad (2.12)$$

$$\mathbf{H}_n(x) = \frac{F_*}{4\pi} A_n(x) \mathbf{\Psi}_n(\Omega, \Omega_0) + \frac{1}{4\pi} \int_0^{2\pi} \int_{-1}^1 \mathbf{I}(x, \Omega') \mathbf{\Psi}_n(\Omega, \Omega') d\mu' d\varphi'. \quad (2.13)$$

Here, we are operating under the plane-parallel approximation, so  $\mu$  is no longer varying with  $z$ , and the integral term in Eq. (2.13) quantifies the diffuse scattering of light into direction  $\Omega = (\mu, \varphi)$  from directions  $\Omega' = (\mu', \varphi')$  over the unit sphere. Scattering matrix  $\mathbf{\Psi}_n(\Omega, \Omega_0)$  is the same as  $\mathbf{\Psi}_n(z)$  in Eq. (2.3), and  $\Omega_0 = (-\mu_0, \varphi_0)$  is the solar direction at the point of scatter. The solar beam attenuation  $A_n(x)$  is treated in the RPS approximation, in which  $A_n(x) = A_n^* e^{-x\lambda_n}$ , where  $A_n^*$  is the ray-traced attenuation to the top boundary of layer  $n$ , and  $\lambda_n$  is an “average secant”. The RPS ansatz allows us to retain a convenient exponential dependence on optical thickness when solving the RTE. For a true plane-parallel medium,  $\lambda = 1/\mu_0$  everywhere. Details of this RPS parameterization may be found in the (V)LIDORT papers.

For each segment and its corresponding layer, the above quadrature scheme  $\{\alpha_j, \chi_j\}$  used for the SS integration (Eqs. 2.7 and 2.8) defines (through spherical trigonometry) a set of  $N_j$  geometries  $G_j = \{\alpha_j, \theta_j, \varphi_j\}$  that will be used (together with the associated layer IOPs) to make a series of  $N_j$  separate VLIDORT calculations, one for each quadrature-point geometrical configuration in the segment. Each such quadrature point on the path has an associated vertical height  $z_j$  and optical thickness  $x_j$ .

Since we are using source function integration as defined by Eq. (2.7), we do not require the post-processing facility normally employed in VLIDORT to carry out optical thickness integrations across layers. Instead, we need only the values of the MS RTE solutions (and not their optically-integrated

counterparts) evaluated for each geometry  $G_j$  at corresponding optical thickness  $x_j$ . We now summarize this evaluation, making careful distinction between the VLIDORT and VLIDORT-QS treatments.

In plane-parallel vector RT, the discrete ordinates RTE solution is simplified by means of Fourier cosine/sine-azimuth expansions of the Stokes 4-vector  $\mathbf{I} = [I, Q, U, V]$  and associated expansions of the  $4 \times 4$  scattering matrices  $\mathbf{\Psi}_n$  in terms of a set of generalized-spherical-function expansion coefficients  $\mathbf{\Gamma}_n$ . For simplicity in the following exposition, we deal with the scalar field  $I$  (no polarization) and the phase function  $\Phi_n$  (which is the (1,1) element of the scattering matrix  $\mathbf{\Psi}_n$ ). The extension to polarized vector fields for VLIDORT follows the same procedure, though the details of vector RT methodology are somewhat more involved, due to the use of scattering matrix entries expressed in generalized spherical function expansions and also the need to take into account complex-valued solutions of the vector RTE [18]. For more on this procedure, refer to the VLIDORT literature, e.g. [11].

Continuing with the scalar case, we write:

$$I_n(\mu, \varphi) = \sum_{m=0}^M (2 - \delta_{m0}) I_n^{(m)}(\mu) \cos m\varphi; \quad (2.14)$$

$$\Phi_n(\Theta) = \sum_{l=0}^M \beta_{nl} P_l(\cos \Theta). \quad (2.15)$$

Eq. (2.15) is the phase-function expansion in terms of Legendre polynomials of the scattering angle, with expansion coefficients  $\{\beta_{nl}\}$ . The resulting Fourier-component RTE for the scalar field is then:

$$\mu \frac{dI_n^{(m)}(x, \mu)}{dx} = -I_n^{(m)}(x, \mu) + \frac{\omega_n}{2} \int_{-1}^1 I_n^{(m)}(x, \mu') \Phi_n^{(m)}(\mu, \mu') d\mu' + P_n^{(m)}(\mu, x); \quad (2.16)$$

$$P_n^{(m)}(\mu, x) = \frac{F_*}{4\pi} A_n^* e^{-x\lambda_n} \omega_n \Phi_n^{(m)}(\mu, -\gamma_n). \quad (2.17)$$

Here,  $P_n^{(m)}(\mu, x)$  is the primary solar scatter term, and we have retained the Fourier index  $m$  and the layer index  $n$ , but not the geometry (segment quadrature) index  $j$ . The phase-function Fourier term  $\Phi_n^{(m)}(\mu, \mu')$  is expressed as products of associated Legendre functions  $P_l^m(\mu)$  and  $P_l^m(\mu')$ , and  $\gamma_n$  is the cosine of the local SZA. In plane-parallel discrete-ordinate RT, solutions to the homogeneous RTE (in the absence of the solar scatter term) are obtained by eigenvalue methods. The RTE particular integral may be obtained either by substitution using the exponential dependency of the RPS approximation or by Green's function methods [11]. Here, we use the former method. Applying these solution methods, the vectors  $\mathbf{I}_n^\pm(x)$  comprise the upwelling (+) and downwelling (-) intensities at discrete ordinate computational quadrature cosines (streams)  $\mu_i, i = 1, \dots, N_d$ , where  $N_d$  is the number of streams in the polar half-space; these intensities are:

$$I_n^\pm(\mu_i, x) = \sum_{p=1}^{N_d} [\mathcal{L}_{np} X_{np}^\pm(\mu_i) e^{-k_{np}x} + \mathcal{M}_{np} X_{np}^\pm(\mu_i) e^{-k_{np}(\Delta_n - x)}] + W_n^\pm(\mu_i) A_n^* e^{-x\lambda_n}. \quad (2.18)$$

The vector elements  $X_{np}^\pm(\mu_i)$  are eigenvectors obtained from the homogeneous-RTE eigenproblem, with separation constants  $k_{np}$ ;  $W_n^\pm(\mu_i)$  are the particular integral solutions. The application of boundary conditions in a multi-layer atmosphere yields integration constants  $[\mathcal{L}_{np}, \mathcal{M}_{np}]$  defined for each eigen-solution  $p$  ( $p = 1, \dots, N_d$ ). Here,  $\Delta_n$  is the complete layer optical thickness in layer  $n$ , and the use of the expression  $e^{-k_{np}(\Delta_n - x)}$  ensures the boundedness of the solutions.

In plane-parallel scattering, we find solutions at any other polar cosine  $\mu$  (away from the discrete ordinate streams) by substituting the discrete ordinate result in Eq. (2.18) into the integral in Eq. (2.16) and performing the subsequent integration using quadrature. This yields the following RTE:

$$\mu \frac{dI_{nm}^{\mp}(x, \mu)}{dx} = -I_{nm}^{\mp}(x, \mu) + J_{nm}^{\mp}(x, \mu) + P_{nm}^{\mp}(\mu, x). \quad (2.19)$$

$$J_{nm}^{\mp}(x, \mu) = \sum_{p=1}^{N_s} [\mathcal{L}_{np} Y_{np}^{\mp}(\mu) e^{-k_{np}x} + \mathcal{M}_{np} Y_{np}^{\pm}(\mu) e^{-k_{np}(\Delta_n - x)}] + Z_n^{\mp}(\mu) A_n^* e^{-x\lambda_n}. \quad (2.20)$$

Scalars  $Y_{np}^{\pm}(\mu)$  and  $Z_n^{\mp}(\mu)$  may be obtained from products of associated Legendre functions  $P_l^m(\mu)$  with components of vectors  $\mathbf{X}_{np}^{\mp}$  and  $\mathbf{W}_n^{\mp}$ ; for details, see [24]. The Fourier index has been suppressed on the right-hand side of (2.20) for the sake of clarity. We are only concerned here with the MS field, so in solving Eq. (2.19) we drop the primary-scatter term  $P_{nm}^{\mp}(\mu, x)$ ; the SS field is determined by an exact treatment in full spherical geometry, as presented in the previous section.

Eq. (2.20) for the radiation solutions  $J_{nm}^{\mp}(x, \mu)$  is our starting point. From here, the MS source term (MSST) developments differ between VLIDORT and VLIDORT-QS.

We start first with the VLIDORT plane-parallel MSSTs. Integrating factors for solving Eq. (2.19) are  $\exp(\pm x/\mu)$ , so that

$$I_{nm}^{\mp}(x, \mu) e^{\pm x/\mu} = \int J_{nm}^{\mp}(y, \mu) e^{\pm y/\mu} dy \quad (2.21)$$

Thus, for example, the upwelling field  $I_{nm}^+(0, \mu)$  at the top of layer  $n$  (optical thickness  $x = 0$  at this point) may be obtained through

$$I_{nm}^+(0, \mu) = I_{nm}^+(\Delta_n, \mu) T_n(\mu) + M_{nm}^+(\mu); \quad (2.22)$$

$$M_{nm}^+(\mu) = \int_{\Delta_n}^0 J_{nm}^+(y, \mu) e^{+y/\mu} dy; \quad T_n(\mu) = \exp\left(-\Delta_n/\mu\right). \quad (2.23)$$

Here,  $T_n(\mu)$  is just the plane-parallel line-of-sight path transmittance in the layer, a quantity dependent only on the vertical optical depth of that layer.  $M_{nm}^+(\mu)$  is the Fourier component of the VLIDORT *MS layer source term*, representing all the light that has been collected along the LOS path from start to finish in that layer. From the expression in Eq. (2.20), we see that the integrations involved in  $M_{nm}^+(\mu)$  are all straightforward exponential expressions, since  $J_{nm}^+(y, \mu)$  has purely exponential dependencies on optical thickness, for eigensolutions  $e^{\pm k_{np}x}$  and particular integral  $e^{-x\lambda_n}$ . Thus, if we substitute the expression for  $J_{nm}^+(y, \mu)$  from Eq. (2.20) into the integral for  $M_{nm}^+(\mu)$  in Eq. (2.23), we find:

$$\begin{aligned} M_{nm}^+(\mu) = & \sum_{p=1}^{N_s} [\mathcal{L}_{np} Y_{np}^{\mp}(\mu) \mathbb{G}_n(\mu, k_{np}) + \mathcal{M}_{np} Y_{np}^{\pm}(\mu) e^{-k_{np}\Delta_n} \mathbb{G}_n(\mu, -k_{np})] \\ & + Z_n^{\mp}(\mu) A_n^* \mathbb{G}_n(\mu, \lambda_n); \quad \mathbb{G}_n(\mu, \lambda) = \frac{1}{(\lambda - \frac{1}{\mu})} \left[ \exp -(\lambda - \frac{1}{\mu})\Delta_n - 1 \right]. \end{aligned} \quad (2.24)$$

For upwelling fields, LOS paths start at the surface, and here we need the reflected intensity at the surface arising from the boundary condition at the bottom of the surface layer  $n = N$ . For Fourier component  $m$  this is given by

$$I_{Nm}^+(\Delta_N, \mu) = + \int_0^1 \mu' R_m(\mu, \mu') I_{Nm}^-(\Delta_N, \mu') d\mu'. \quad (2.25)$$

The LIDORT solution for a given Fourier component is then finished by applying the recursion formula in Eq. (2.22) on a layer-by-layer basis to compute the Fourier-component field at the desired output level. For the downwelling recursion, the field is zero at the top of the atmosphere (no downwelling diffuse radiation); for the upwelling case, the recursion starts with the surface field (2.25). Once this recursion is done, the Fourier cosine-azimuth series in Eq. (2.13) is then applied, whereby new (fully-recursed) Fourier-component contributions are added until the azimuth series converges up to a prescribed level of accuracy. The procedure for VLIDORT is the same, though the algebra is necessarily more complex.

Now we look at the post-processing treatment for VLIDORT-QS. As noted in the introduction, the optical depth integration here will be done using the *spherical-path* quadrature gridding developed for the SS solution. Therefore, our starting point is the expressions  $J_{nm}^\mp(x_j, \mu_j)$  from Eq. (2.20) now evaluated at the spherical-path quadrature grid points  $\{x_j, \mu_j\}$ . Before moving to the optical depth integration, we first execute the Fourier series azimuth convergence directly on the MS terms in Eq. (2.20). Thus, for scalar RT, we have the azimuth-converged MS field for geometry  $G_q = \{\alpha_j, \theta_j, \varphi_j\}$  and optical thickness  $x_j$ :

$$I_{nj}^\mp(x_j, \mu_j, \varphi_j) = \sum_{m=0}^M (2 - \delta_{m0}) J_{nm}^\mp(x_j, \mu_j) \cos m\varphi_j. \quad (2.26)$$

These are scalar expressions. For polarized RT, the Fourier-summed vector equivalents  $\mathbf{I}_{nj}^\mp(x_j, \mu_j, \varphi_j)$  of the scalar quantities in Eq. (2.26) will involve sine and cosine series expansions. These fields are the basic quantities we take from our specially-adapted form of VLIDORT for the MS field, and from now on we revert back to the vector exposition.

The optical thickness source function integrations for the MS fields are now done using the quantities  $\mathbf{I}_{nj}^\mp(x_j)$  and the quadrature scheme  $\{x_j, \mu_j\}$  from the SS calculation. Thus, for the complete (SS+MS) upwelling field in segment  $s$ , we may write:

$$\mathbf{I}_s^\uparrow = T_s \mathbf{I}_{s-1}^\uparrow + \mathbf{L}_s^\uparrow + \mathbf{M}_s^\uparrow; \quad \mathbf{M}_s^\uparrow = \sum_{j=1}^{N_j} f_n(\alpha_j) \mathbf{I}_{nj}^\uparrow(x_j). \quad (2.27)$$

Following the notation in Eq. (2.9), the full Stokes vector  $\mathbf{I}_{cam}$  at the camera is now

$$\mathbf{I}_{cam} = \sum_{s=1}^{N_s} C_{s-1} (\mathbf{L}_s + \mathbf{M}_s). \quad (\text{Regimes II and III}) \quad (2.28)$$

For Regime I, there are additional considerations arising from surface reflection. In addition to the Fourier-summed upwelling VLIDORT MS field at the surface, it is necessary to evaluate the Fourier-summed downwelling field at the surface, and then apply the reflectance boundary condition to generate an additional contribution to the surface upwelling field. Once done, the total surface upwelling field is then propagated upwards to the target using the cumulative transmittance (just as in the SS case). Confining attention to a Lambertian surface with albedo  $R$  for which reflection only applies in the azimuth-independent Fourier-zero contribution, the total upwelling MS surface reflection field is now:

$$\mathbf{I}_{Surf}^{(MS)}(\mu) = \int_0^1 \mu' \mathbf{R} \mathbf{I}_n^{\downarrow(0)}(\mu', \Delta_n) d\mu'. \quad (2.29)$$

Here,  $\mathbf{R}$  is the 4×4 reflection matrix with only the (1,1) element taking the Lambertian albedo value  $R$ ;  $\Delta_n$  is the optical thickness of the lowest layer of the atmosphere;  $\mathbf{I}_n^{(0)}(\mu, \Delta_n)$  is the Fourier-zero component of the downwelling Stokes vector at the surface. The reflection integral in (2.29) is evaluated using discrete ordinate quadrature, based on values  $\mathbf{I}_n^{(0)}(\mu_p, \Delta_n)$  of the downwelling field at ordinates  $\mu_p, p = 1, \dots, N_d$ . Using this, the final result for a Regime I calculation is:

$$\mathbf{I}_{cam} = C_{N_s} \{ \mathbf{I}_{Surf}^{(DB)} + \mathbf{I}_{Surf}^{(MS)} \} + \sum_{s=1}^{N_s} C_{s-1} (\mathbf{L}_s^\dagger + \mathbf{M}_s^\dagger). \quad (\text{Regime I}). \quad (2.30)$$

**Remark.** The SS field is derived using the *complete* scattering phase matrix, not the *truncated* form arising from the discrete ordinates approximation. When delta-M scaling is applied to the MS RTE, we invoke the Nakajima-Tanaka TMS correction *ansatz* for the SS computation [25]. The Nakajima-Tanaka procedure uses *unscaled* scattering properties in the SS RTE, along with *scaled* extinctions  $\bar{k}_n$ , with the source term in each layer further divided by the factor  $(1 - \omega_n \zeta_n)$ , where  $\omega_n$  is the unscaled total single scatter albedo in layer  $n$ , and  $\zeta_n$  is the delta-M scaling truncation factor. Details on the delta-M scaling procedure in LIDORT may be found in the literature (see e.g. [24]).

### 2.3. Linearizations of the RT model

In order to facilitate retrievals from airborne and satellite spectrometer measurements, VLIDORT-QS has been given the full capability to deliver profile Jacobians (weighting functions) with respect to any layer optical quantity (such as trace gas absorption optical thickness, ice-cloud/aerosol/water-cloud optical thickness profiles, etc.). As long as the partial derivatives of the IOPs with respect to these profile quantities have been specified, the linearization capabilities in both the SS and MS parts of VLIDORT-QS will ensure that the associated analytically-derived profile Jacobians are delivered alongside the Stokes vectors. Here, we summarize the Jacobian derivations, which are based closely on the treatments in LIDORT and VLIDORT.

The IOPs  $\{k_n, \omega_n, \mathbf{\Gamma}_n\}, n = 1, \dots, N_L$ , defined in Section 2.1, are the basic inputs to VLIDORT-QS. We now define a set of associated linearized IOPs:

$$\mathbb{V}_n = \frac{\partial k_n}{\partial \xi_n}; \quad \mathbb{W}_n = \frac{\partial \omega_n}{\partial \xi_n}; \quad \mathbb{G}_n = \frac{\partial \mathbf{\Gamma}_n}{\partial \xi_n}. \quad (n = 1, \dots, N_L). \quad (2.31)$$

Here,  $\xi_n$  is a layer atmospheric quantity for which we wish to define a Jacobian. As was the case with the regular RT problem, we need to derive the quantities  $\mathbb{Y}_n = \partial \mathbf{\Psi}_n / \partial \xi_n$  for the linearized problem, from the generalized spherical functions and the inputs  $\mathbb{G}_n = \partial \mathbf{\Gamma}_n / \partial \xi_n$ . Here,  $\mathbb{V}_n, \mathbb{W}_n$ , and  $\mathbb{Y}_n$  will be required for the linearized SS code, while  $\mathbb{V}_n, \mathbb{W}_n$ , and  $\mathbb{G}_n$  will be needed as inputs to the linearized MS part of VLIDORT-QS. We use the following notation for Jacobians:

$$\mathbf{K}_{s,n} \equiv \mathbb{L}_n[\mathbf{I}_s] \equiv \frac{\partial \mathbf{I}_s}{\partial \xi_n}. \quad (2.32)$$

Dealing first with the SS code, we take the partial derivative of Eq. (2.3) with respect to parameter  $\xi_q$  in layer  $q$ :

$$\mathbb{L}_q[\mathbf{H}_n(z)] = \frac{F_*}{4\pi} \{ \mathbb{L}_q[A_n(z)] \mathbf{\Psi}_n(z) + A_n(z) \delta_{nq} \mathbb{Y}_n(z) \}; \quad (2.33)$$

$$\mathbb{L}_q[A_n(z)] = -d_{nq}(z) \mathbb{V}_q A_n(z). \quad (2.34)$$

Notice the presence of cross-layer derivatives in the second of these two equations ( $\delta_{nq}$  in Eq. (2.33) is the Kronecker delta symbol). Continuing, we now differentiate Eq. (2.4), (2.6) – (2.8) as follows (going straight for the LOS quadrature scheme representation of the source term):

$$\mathbb{L}_q[\mathbf{I}_s^\uparrow] = \mathbb{L}_q[T_s]\mathbf{I}_{s-1}^\uparrow + T_s\mathbb{L}_q[\mathbf{I}_{s-1}^\uparrow] + \mathbb{L}_q[\mathbf{L}_s^\uparrow]; \quad (2.35)$$

$$\mathbb{L}_q[T_s] = -C\mathbb{V}_q\delta_{nq}y(\alpha_s)T_s. \quad (2.36)$$

$$\mathbb{L}_q[\mathbf{L}_s^\uparrow] = \sum_{j=1}^{N_j} f_n(\alpha_j)\mathbb{L}_q[\mathbf{H}_n(\alpha_j)] + \mathbb{L}_q[f_n(\alpha_j)]\mathbf{H}_n(\alpha_j); \quad (2.37)$$

$$\mathbb{L}_q[f_n(\alpha_j)] = \chi_j\delta_{nq}\frac{\exp[-Ck_n y(\alpha_j)]}{\sin^2 \alpha_j}[\mathbb{W}_n - C\mathbb{V}_n y(\alpha_j)]. \quad (2.38)$$

Here, we have used the shorthand  $y(\alpha) = \cot \alpha - \cot \alpha_{s-1}$ .

Now we can get the SS Jacobians for the final results for Regimes II and III. Indeed:

$$\mathbf{K}_{cam,q} \equiv \mathbb{L}_q[\mathbf{I}_{cam}] = \sum_{s=1}^{N_s} \mathbb{L}_q[C_{s-1}]\mathbf{L}_s + C_{s-1}\mathbb{L}_q[\mathbf{L}_s]; \quad (2.39)$$

$$\mathbb{L}_q[C_s] = C_s \sum_{k=1}^s \frac{\mathbb{L}_q[T_k]}{T_k} \quad (s > 0); \quad \mathbb{L}_q[C_0] = 0. \quad (2.40)$$

We complete the SS linearization by finding derivatives of the surface direct-bounce term:

$$\mathbb{L}_q[\mathbf{I}_{N_s}^{(DB)}] = \mathbb{L}_q[C_{N_s}]\mathbf{I}_{Surf}^{(DB)} + C_{N_s}\mathbb{L}_q[\mathbf{I}_{Surf}^{(DB)}]; \quad \mathbb{L}_q[\mathbf{I}_{Surf}^{(DB)}] = F_* \frac{R\mu_0}{\pi} \mathbb{L}_q[A_{surf}(\mu_0)]. \quad (2.41)$$

We turn now to the MS Jacobians, relying on the VLIDORT linearization. Here we will not repeat VLIDORT differentiation, quoting results as they are needed for the new model. For ease of exposition, we again work with the scalar field.

Our starting point is the discrete ordinate solution in layer  $n$  in Eq. (2.18). Formal differentiation with respect to parameter  $\xi_q$  in layer  $q$  yields:

$$\begin{aligned} \mathbb{L}_q[\mathbf{I}_n^\mp(x)] &= \sum_{p=1}^{N_d} [\mathcal{N}_{npq}\mathbf{X}_{np}^\mp e^{-k_{np}x} + \mathcal{P}_{npq}\mathbf{X}_{np}^\pm e^{-k_{np}(\Delta_n-x)}] + \\ &\quad \delta_{nq} \sum_{p=1}^{N_d} [\mathcal{L}_{np}\mathbb{L}_n[\mathbf{X}_{np}^\mp e^{-k_{np}x}] + \mathcal{M}_{np}\mathbb{L}_n[\mathbf{X}_{np}^\pm e^{-k_{np}(\Delta_n-x)}]] + \\ &\quad \mathbb{L}_q[\mathbf{W}_n^\mp]A_n^*e^{-x\lambda_n} + \mathbf{W}_n^\mp \mathbb{L}_q[A_n^*e^{-x\lambda_n}]. \end{aligned} \quad (2.42)$$

In the second term on the right-hand side, linearizations of the homogeneous RTE solutions  $\{k_{np}, \mathbf{X}_{np}^\mp\}$  do not depend on parameters outside layer  $n$ ; there are no cross derivatives. In the first term,  $\{\mathcal{N}_{npq}, \mathcal{P}_{npq}\}$  are linearizations of the integration constants  $\{\mathcal{L}_{np}, \mathcal{M}_{np}\}$ , found by taking derivatives of the boundary value problem. In the remaining terms, linearizations  $\mathbb{L}_q[\mathbf{W}_n^\mp]$  are found by differentiating the linear matrix algebra equations that determine the particular integrals  $\mathbf{W}_n^\mp$ , while the derivative  $\mathbb{L}_q[A_n^*e^{-x\lambda_n}]$  of the pseudo-spherical “average-secant” solar beam attenuation will depend only on the linearized IOP  $\mathbb{V}_q$ .

Both these particular-integral terms have cross-layer derivatives. Procedures and detailed derivations of all of these linearization steps may be found in the LIDORT and VLIDORT papers.

Moving on to the MS fields in Eq. (2.19) at specific off-stream directions and optical thickness values  $\{\mu_j, x_j\}$  required for the recursion, we require additional linearizations of the homogeneous solutions  $Y_{njp}^\mp(\mu_j)$  and particular-integral values  $Z_{nj}^\mp(\mu_j)$ . Again, procedures for these derivatives can be found in the LIDORT papers, and we will not write them down here. Once known, it is easy to derive the Fourier-summed linearizations  $\mathbb{L}_q[I_{nj}^\mp(x_j)]$  for the scalar solution, and equivalents  $\mathbb{L}_q[\mathbf{I}_{nj}^\mp(x_j)]$  for the VLIDORT problem with polarization. We take this as done.

The rest of the linearization process for the MS contributions then follows much the same track as that for the SS calculation, since we already have linearizations of the segment and cumulative transmittances  $T_s$  and  $C_s$  respectively, plus a linearization  $\mathbb{L}_q[f_n(\alpha_j)]$  of the quadrature integration. From Eq. (2.27), we have for the full SS + MS recursion:

$$\mathbb{L}_q[\mathbf{I}_s^\uparrow] = \mathbb{L}_q[T_s]\mathbf{I}_{s-1}^\uparrow + T_s\mathbb{L}_q[\mathbf{I}_{s-1}^\uparrow] + \mathbb{L}_q[\mathbf{L}_s^\uparrow] + \mathbb{L}_q[\mathbf{M}_s^\uparrow]; \quad (2.43)$$

$$\mathbb{L}_q[\mathbf{M}_s^\uparrow] = \sum_{j=1}^{N_j} f_n(\alpha_j)\mathbb{L}_q[\mathbf{I}_{nj}^\uparrow(x_j)] + \mathbb{L}_q[f_n(\alpha_j)]\mathbf{I}_{nj}^\uparrow(x_j). \quad (2.44)$$

Now we can get the SS+MS Jacobians for the final results for Regimes II and III. Indeed, differentiation of Eq. (2.28) yields:

$$\mathbf{K}_{cam,q} \equiv \mathbb{L}_q[\mathbf{I}_{cam}] = \sum_{s=1}^{N_s} \mathbb{L}_q[C_{s-1}](\mathbf{L}_s + \mathbf{M}_s) + C_{s-1}(\mathbb{L}_q[\mathbf{L}_s] + \mathbb{L}_q[\mathbf{M}_s]). \quad (2.45)$$

It remains to derive the Jacobian surface-reflected contributions in Regime I. From Eq. (2.29), a formal linearization yields:

$$\mathbb{L}_q[\mathbf{I}_{Surf}^{(MS)}] = \int_0^1 \mu \mathbf{R} \mathbb{L}_q[\mathbf{I}_n^{\downarrow(0)}(\mu, \Delta_n)] d\mu. \quad (2.46)$$

The derivatives in this equation follow from the VLIDORT linearization. The final Regime I Jacobian at the camera follows easily from this result and a differentiation of Eq. (2.30).

**Remark.** The Nakajima-Tanaka TMS correction process for SS and MS fields is fully differentiable. It depends on the use of delta-M scaled optical properties - these quantities are differentiable in terms of the basic set of linearized IOPs in Eq. (2.31). For details, see for example [24] for the scalar field.

### 3. Examples and Validation of the VLIDORT-QS model

#### 3.1. Comparisons with standard VLIDORT

This validation is important to check for consistency. For nadir-upwelling and nadir-downwelling scenarios with LOS paths that are not too far from the zenith, we expect rather close agreement between VLIDORT-QS results and those from standard VLIDORT simulations; here, LOS sphericity effects are generally small or minimal. For this test, the standard VLIDORT model is executed in the EPS mode, with solar beam attenuation always treated for a curved atmosphere, and with a fully accurate spherical SS calculation. We can improve upon this validation by considering the MS source term sphericity corrections recently applied to VLIDORT in the context of spherical-code benchmarking [17].

In “standard” VLIDORT operating in the EPS mode, the MS portion of the RT solution is treated in plane-parallel geometry (i.e. the solar and viewing geometry does not vary from layer to layer). For the alternative options in VLIDORT to use either the 2-point, 3-point, or multi-point sphericity correction, the path geometry is allowed to vary for the MS portion of the RT calculation. These sphericity corrections were introduced for the first time in VLIDORT Version 2.8.3, which at the time of writing is still the most recent official release of the code.

The 2-point sphericity correction was described briefly in the Introduction. Here, MS path source term integrations are performed for just 2 geometries at the top and bottom of the atmosphere, and at intermediate geometrical configurations, other MS source terms are obtained by interpolation (against the cosine of the viewing zenith angle). For the 3-point correction, 3 path geometries are selected for the MS source term computations, with values at intermediate geometrical configurations again obtained by interpolation. The multi-point correction will determine source-terms at all layer-boundary path geometries; this is a slower procedure but the most accurate, as interpolation errors will be very small in this case. For more details on these corrections, please refer to [17] and [29].

We take an upwelling satellite reflectance scenario in a clear-sky (no aerosol) atmosphere, with a total Rayleigh scattering optical thickness of 0.867 and a total ozone absorption optical thickness of 0.087; these values are typical for the UV spectrum around 325 nm. There are 23 layers in all with height resolutions 1 km from 0–10 km, 2 km from 10–24 km, and 3–5 km thereon up to the TOA at 60 km (the location of the camera). Results are obtained for scalar radiation (no polarization) with eight discrete ordinates. The standard EPS calculation involves just a single call to VLIDORT, with a single SZA of 81°, a single azimuth (0°) corresponding to viewing in the principal plane, and a range of 81 LZAs running from 0–80°. We also run these geometrical configurations for the modified forms of VLIDORT using 2-point, 3-point and multi-point sphericity corrections, as outlined in the Section 1 of this paper and discussed in [17]. Lastly, these configurations are then run with the VLIDORT-QS model.

**Table 3.1.** Results from VLIDORT Standard EPS, VLIDORT with 2-point spherical correction (SC), VLIDORT with 3-point SC, VLIDORT with multi-point SC, and VLIDORT-QS (VQS).

VZA	Single Scatter	Multiple Scatter Intensities					% Difference vs. VLIDORT_QS			
		Ims_Std	Ims_2pt	Ims_3pt	Ims_Mpt	Ims_VQS	Std	2pt	3pt	Mpt
10.0	0.005458	0.00795	0.00794	0.00794	0.00794	0.00794	-0.188	-0.000	-0.000	-0.000
20.0	0.005852	0.00818	0.00815	0.00815	0.00815	0.00815	-0.400	-0.001	-0.000	-0.000
30.0	0.006764	0.00858	0.00853	0.00853	0.00853	0.00853	-0.658	-0.003	-0.000	-0.000
40.0	0.008288	0.00917	0.00908	0.00908	0.00908	0.00908	-1.002	-0.008	-0.002	-0.000



50.0	0.010594	0.00996	0.00982	0.00982	0.00981	0.00981	-1.500	-0.021	-0.006	-0.001
60.0	0.013995	0.01093	0.01069	0.01069	0.01069	0.01069	-2.305	-0.065	-0.021	-0.002
65.0	0.016270	0.01144	0.01113	0.01111	0.01111	0.01111	-2.295	-0.123	-0.040	-0.004
70.0	0.019054	0.01187	0.01146	0.01144	0.01144	0.01144	-3.799	-0.262	-0.084	-0.006
72.0	0.020332	0.01198	0.01154	0.01151	0.01150	0.01149	-4.248	-0.370	-0.118	-0.007
74.0	0.021707	0.01204	0.01155	0.01151	0.01149	0.01149	-4.765	-0.543	-0.171	-0.009
76.0	0.023172	0.01200	0.01149	0.01142	0.01139	0.01139	-5.350	-0.831	-0.258	-0.011
78.0	0.024706	0.01183	0.01132	0.01121	0.01117	0.01116	-5.978	-1.340	-0.407	-0.015
80.0	0.026256	0.01147	0.01101	0.01084	0.01077	0.01076	-6.556	-2.306	-0.681	-0.022

Columns 2 (SS: single-scatter) and 3–7 (MS: multiple-scatter) in Table 3.1 contain values of the sun-normalized TOA upwelling intensity contributions for a selection of (BOA) LZAs as seen in Column 1. The SS calculation is always done with full spherical geometry; for SS, VLIDORT EPS results agree with those from VLIDORT-QS to better than seven decimal places. We are therefore only interested in differences in MS contributions. Relative differences (in %) between VLIDORT MS results (with and without the various sphericity corrections) and VLIDORT-QS MS values are shown in columns 8–11. It is clear that for increasingly wide-angle views away from direct nadir, VLIDORT running in standard mode is biased high by several percent. Running VLIDORT with the 2-pt and 3-pt sphericity corrections give results similar to those from VLIDORT-QS, at least for camera angles up to 60°; thereafter, the 2-pt and 3-pt SC results differ more widely from those of VLIDORT-QS. For the multi-point SC comparisons in column 11, results are very close to those from VLIDORT-QS, as one would expect when treating the MS layer source terms on a layer-by-layer (or more accurately, segment-by-segment) basis.

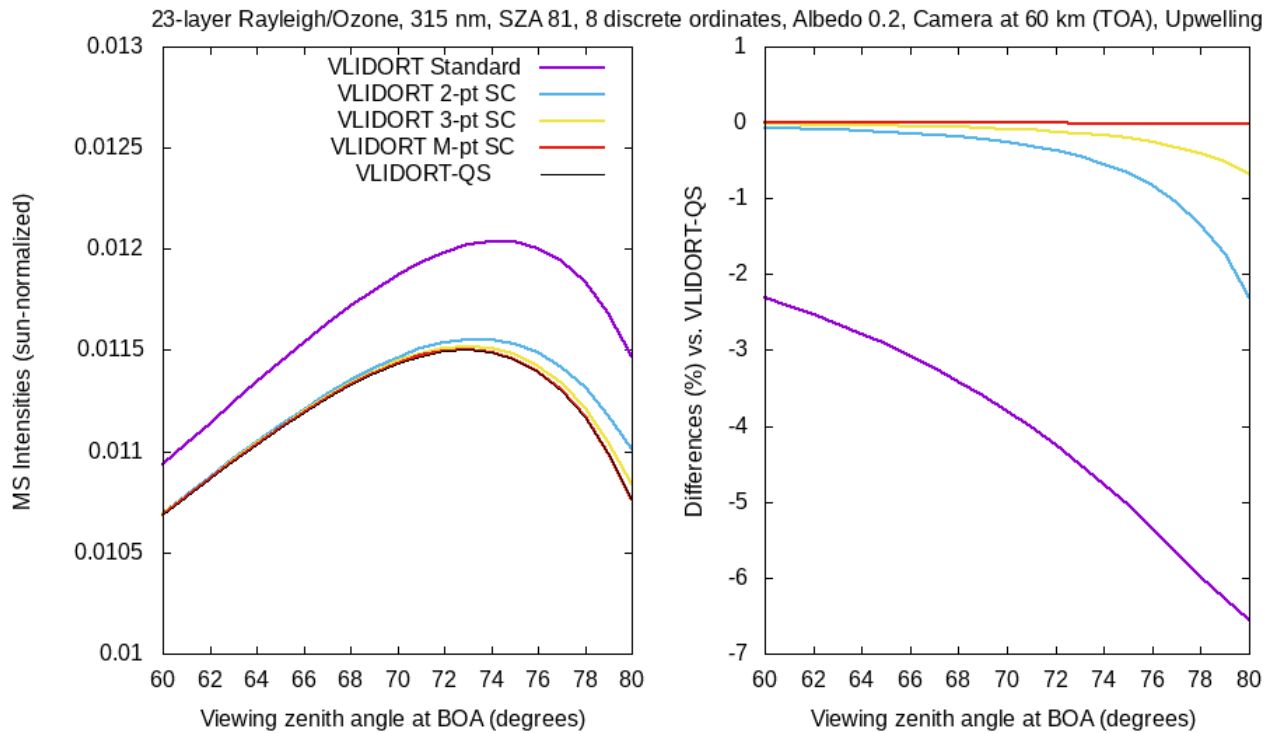


**Figure 3.1.** Multiple-scatter TOA-upwelling intensities for VLIDORT (with and without sphericity corrections) and VLIDORT-QS. Relative differences to VLIDORT-QS are shown in the right panel.

These results are displayed in graphical form in Figure 3.1. The left panel shows MS TOA intensities for LZA values above  $60^\circ$ ; the high bias of the standard VLIDORT result is apparent. The right plot is an extension of columns 8–11 in Table 3.1. Differences between the VLIDORT multi-point correction results and those from VLIDORT-QS are very small indeed: better than  $10^{-4}$  for LOS angles up to  $76^\circ$ .

The 2-point correction compensates very well for changes in MS geometry for LZAs up to  $60^\circ$  from zenith. It should be noted here that the 2-point and 3-point sphericity corrections are simple to implement in the VLIDORT model, and they are now a standard feature of the latest official VLIDORT RT package from RT Solutions (Version 2.8.3 of VLIDORT, release date August 2021). Interested readers should contact Robert Spurr at RT Solutions.

We now move on to validation for more spherical geometrical configurations, including limb-viewing scenarios, which is something that is beyond the scope of standard VLIDORT, even with sphericity corrections applied. We consider two Earth atmosphere scenarios, the first for a pure Rayleigh atmosphere, then a second case with a high-level stratospheric aerosol layer.

### 3.2. Monte Carlo validation

The initial validation tests for limb and near-limb geometrical scenarios were done with the McArtim Monte Carlo (MC) spherical code [3]. These comparisons were performed for a number of scenarios, including a Rayleigh-only atmosphere, and for camera positions in the stratosphere in the presence of high-altitude clouds. These tests were specifically designed to provide meaningful model comparisons, and as such, they were not based on actual data or observations. Our results showed average differences with this MC output on the order of 3% or less, depending on the geometry and the scenario.

Unfortunately, the McArtim code is no longer supported, and for the validation, we have therefore turned to the MYSTIC MC model [4], which is actually one component of the publicly-available state-of-the-art “libRadtran” package [7]. MYSTIC is a 1-D or 3-D MC code for polarized RT; it can use either the “forward” or “backward” Monte Carlo technique, with photons traced from source to detector or vice-versa [26,27]. The MC simulations can also use the so-called Variance Reduction Optimal Options Method (VROOM) [28]. MYSTIC can also perform plane-parallel RT, but in our work, we use it for spherical 1-D simulations, with tracing calculations performed with 1 Million or 100 Million photons.

Although the aim is to compare our model directly with this MC code, we note in passing that MYSTIC has already been used to validate the 2-point sphericity correction applied to VLIDORT [17] and again for the multi-point sphericity correction [29]. For the 2-point validation, the benchmarking was done for 100-layer pure Rayleigh scattering atmospheres of total optical thicknesses 0.25 and 1.0, and for a zero-albedo (dark) surface. Scenarios were confined to scalar RT (no polarization) in the principal plane for upwelling intensities at TOA. It was shown in this work that application of the 2-point MS correction to standard VLIDORT output yields agreement with MYSTIC results to better than 1% for a wide range of viewing angles and SZAs up to 80 degrees [17]. In the second validation for the multi-point sphericity correction, numerical results were presented for polarizing Rayleigh atmospheres at two total optical depths (0.25 and 1.0), with and without an absorption profile, for cosine SZAs 0.1 and 0.9, relative azimuth angles  $0^\circ$ ,  $90^\circ$  and  $180^\circ$ , and viewing zenith angles from  $0^\circ$  to  $87^\circ$ . Excellent agreement was observed in the comparisons between VLIDORT with the multi-point correction and the full-spherical MYSTIC model; most of the differences in top-of-atmosphere radiances were found to be in the range  $\pm 0.2\%$  for these geometries [29].

For the VLIDORT-QS comparisons, we first look at a more physically realistic pure Rayleigh scattering atmosphere with 40 layers having equal geometrical thickness (1.5 km) from 0 to 60 km. The total optical

thickness is 0.5, but (unlike the benchmarking noted above) layer optical thickness values are directly related to air column densities, with temperature and pressure profiles interpolated from the AFGL US standard atmosphere [30]. Both VLIDORT-QS and MYSTIC will ingest this Rayleigh optical thickness profile “as is”, though MYSTIC does require pressure and temperature profiles for the ray tracing.

We consider two placements of the camera. The first is at TOA (60 km) for 12 LZA viewing positions: seven upwelling ground-reflection and five limb-viewing configurations (Regimes I and II in VLIDORT-QS). The second placement is inside the atmosphere at 16.5 km for 18 LZA viewing positions where all three Regimes (direct upwelling, direct downwelling, and limb views) are encountered (six positions each). Table 3.2 shows these camera viewing angles; they have been chosen as representative for the ray-tracing regimes involved. Results are given for five different SZAs (30°, 50°, 70°, 80°, 85°) in the principal plane and two albedo values (0.0 and 0.25). Calls to VLIDORT-QS use either four or eight polar streams in the half-space; this is accurate enough for Rayleigh scattering [31].

**Table 3.2.** Viewing scenarios for comparisons with MYSTIC.

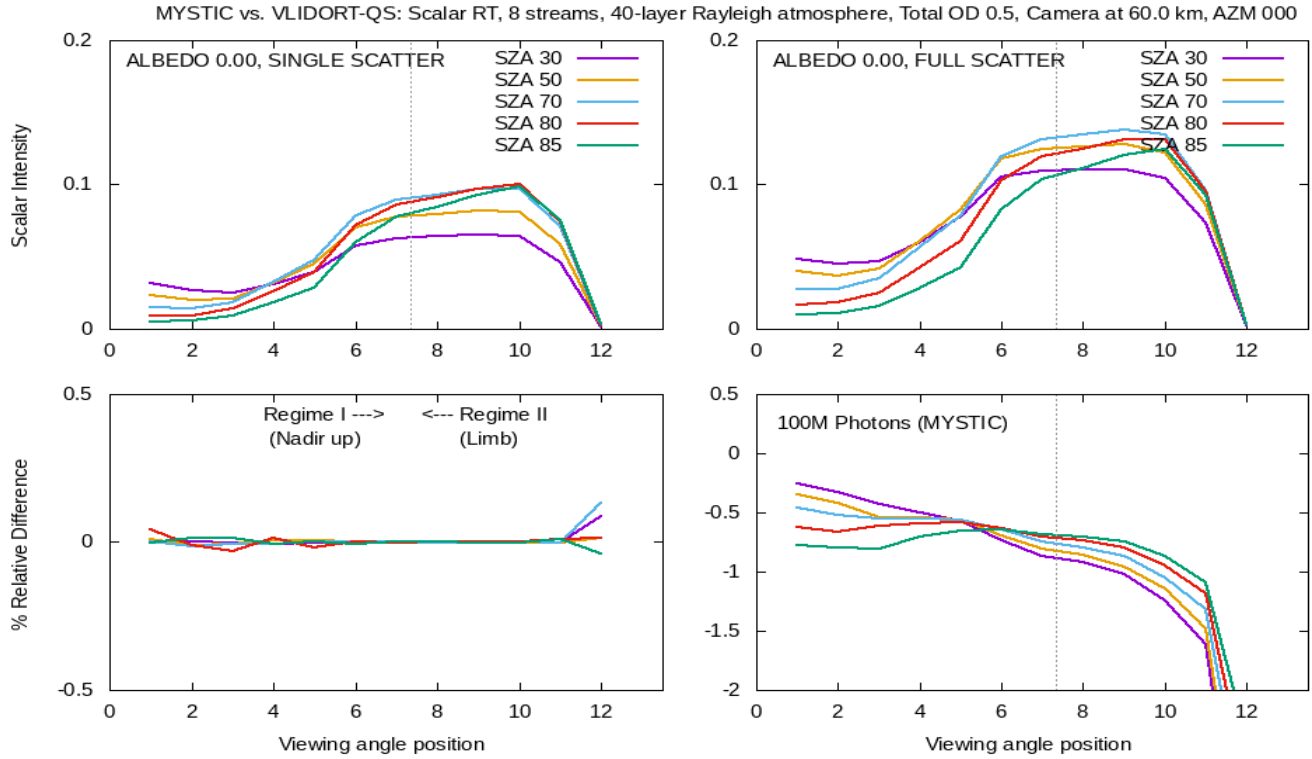
Camera height	Viewing Conditions (zenith angles and Regimes). [Angles in degrees]																		
60.0 km	angle	0	20	40	60	70	80	82	82.5	83	83.5	84	86						
	regime	I	I	I	I	I	I	I	II	II	II	II	II						
16.5 km	angle	0	20	40	60	80	85	85.5	86	86.5	87	89	90	91	93	110	130	150	180
	regime	I	I	I	I	I	I	II	II	II	II	II	II	III	III	III	III	III	III

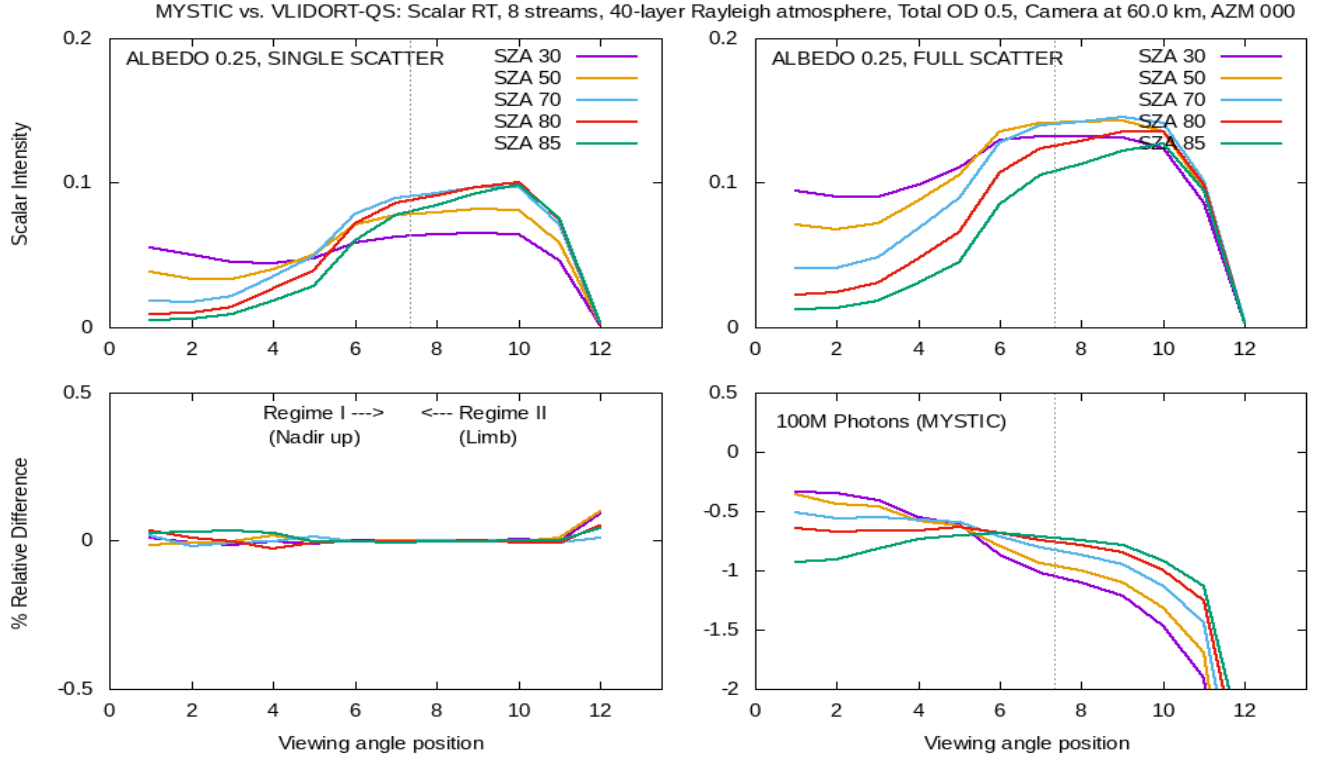
Results for both the SS and the full (SS+MS) radiation fields are shown in Figures 3.2 to 3.4. Comparisons are shown with MYSTIC calculations using 100 Million photons; this reduced the statistical error considerably when compared with MYSTIC outputs based on 1 Million photons.

MYSTIC 100M-photon calculations were performed on a cluster of 10 CPUs (Intel(R) Xeon(R) Gold 6262V CPU @ 1.90GHz, 2 threads per core) using a Python environment. Timings for full radiation field calculations are roughly 1.5 times longer than those for SS computations. The full calculations took 4–6 hours to execute for the camera at 16.5 km scenarios, and 3–5 hours for the camera position at 60 km. The VLIDORT-QS calculations were performed on a single Desktop (Dell XPS 8930, Intel(R) Core I7 8700 @ 3.20 GHz) using only one core; they took roughly two minutes for the camera at 60 km using eight discrete ordinates in the polar half-space, and three minutes for the camera at 16.5 km. Performance speed-up with VLIDORT-QS is better than two orders of magnitude, and this will become around three orders of magnitude using multiple (8 or more) cores, since the VLIDORT-QS software is thread-safe and therefore suitable for use with parallel-computing constructs such as OpenMP. We note that these performance figures are approximate, since the Python environment calling MYSTIC does not reveal the distribution of runs among the cores and threads. A more accurate figure can be obtained by running both codes on a single CPU operating with eight cores. Figure 3.2 has the validation for the first camera placement (TOA upwelling at 60 km) for two sets of albedos. There are seven results for Regime I and five for Regime II (positions 1–12 in the plots). The Regime change occurs at a critical angle 85.38°. Plots on the left display the SS results, those on the right are the full-field radiance and comparisons. VLIDORT-QS intensities are shown in the upper plots, and relative differences against MYSTIC in the lower plots.

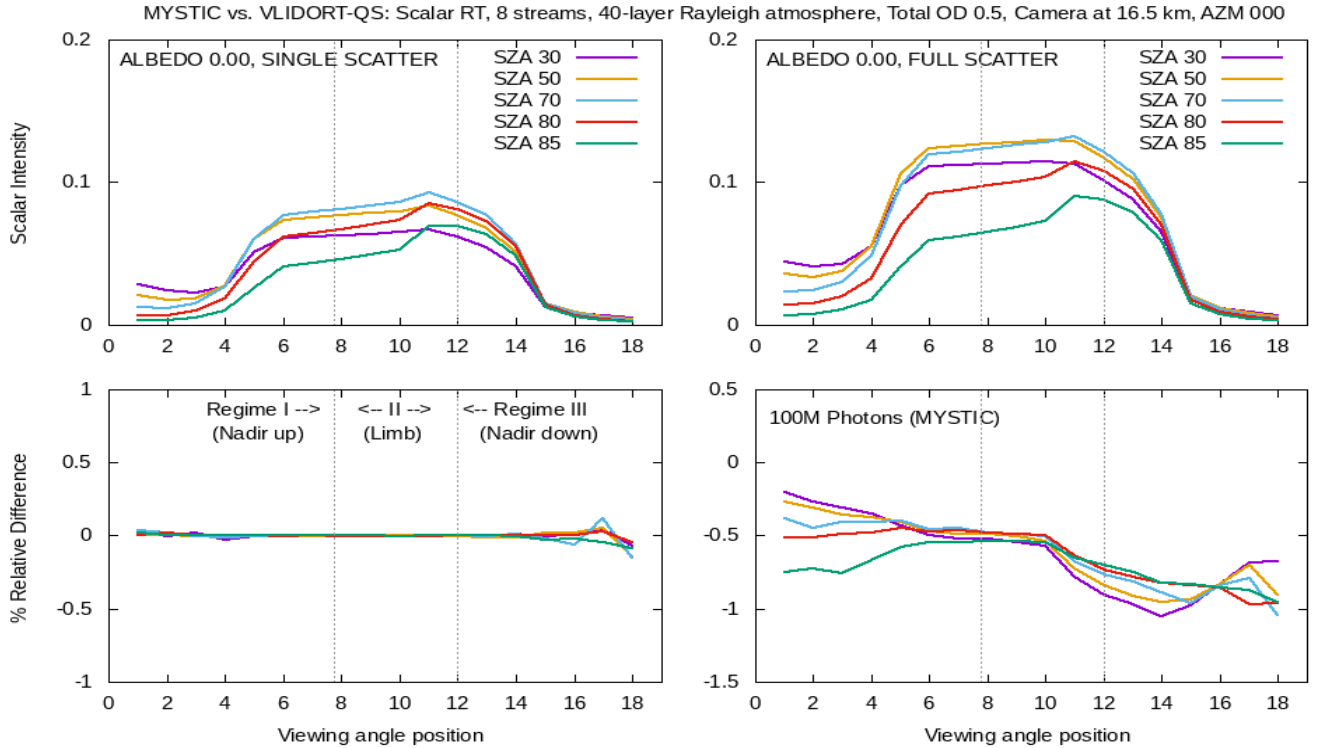
Differences in the SS results are insignificant for both albedo values. For the dark surface, agreements are better than 1% in all Regime I cases and most Regime II cases, becoming slightly worse for the two uppermost limb-viewing scenarios. There is clear bias present – in virtually all cases, VLIDORT-QS will overestimate the intensity; the bias is about 0.6% for the zero-albedo case, and slightly worse (~0.8%) for

albedo 0.25. This bias is a horizontal sphericity effect. MS VLIDORT-QS calculations are plane-parallel, with infinite horizontal extent for the atmosphere, whereas in the MC code, the atmosphere is finitely spherical.





**Figure 3.2.** Comparisons of VLIDORT-QS against MYSTIC MC model, scalar RT, for camera at 60 km and two sets of surface albedos: 0.0 (upper four panels) and 0.25 (lower four panels). VLIDORT-QS results in each set are for (top left) SS and (top right) full radiance fields. Relative differences between VLIDORT-QS and MYSTIC are for (bottom left) SS and (bottom right) full radiance fields.



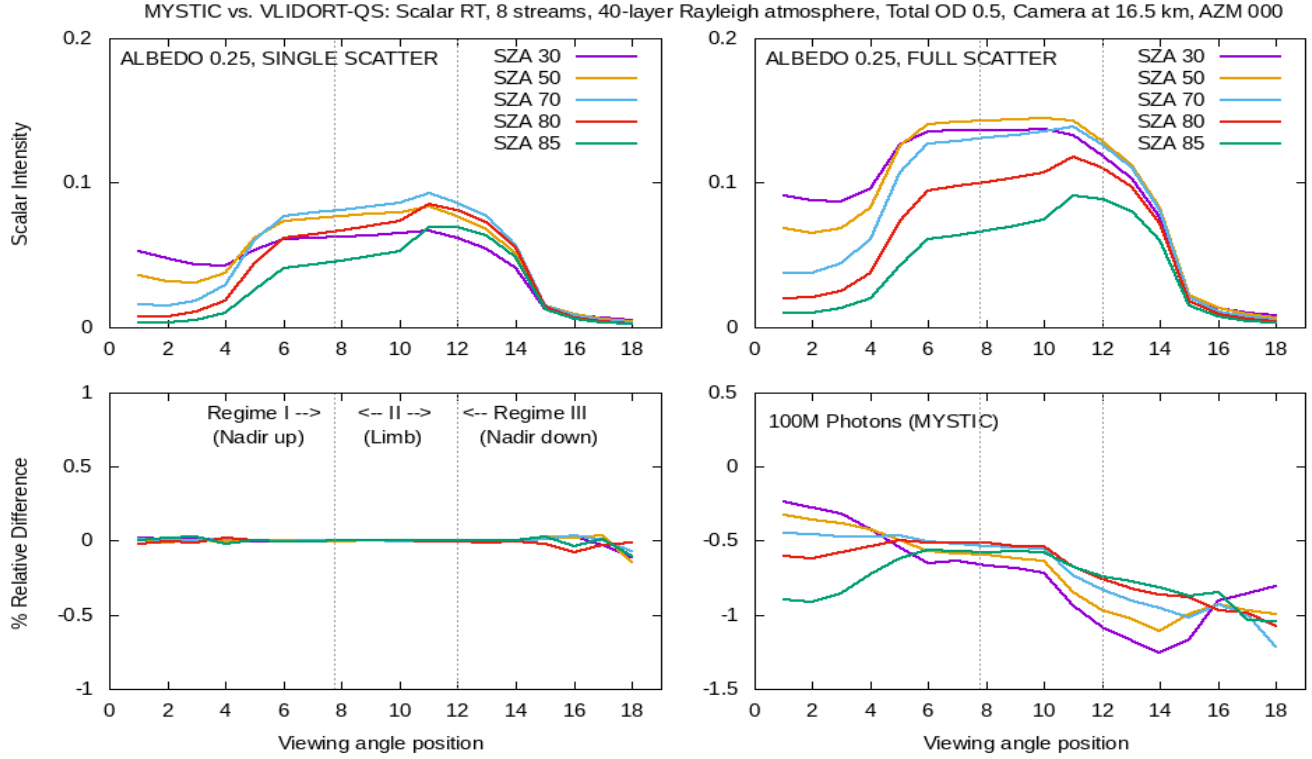


**Figure 3.3.** Comparisons of VLIDORT-QS against MYSTIC MC model, scalar RT for camera at 16.5 km and two sets of surface albedos: 0.0 (upper four panels) and 0.25 (lower four panels). VLIDORT-QS results in each set are for (top left) SS and (top right) full radiance fields. Relative differences between VLIDORT-QS and MYSTIC are for (bottom left) SS and (bottom right) full radiance fields.

Results for the second camera placement are shown in Figure 3.3. There are more viewing positions, as it is now possible to move the camera from pointing straight down (position 1) to straight up (position 18), moving through a number of viewing configurations; the Regime I/II change takes place at critical angle  $82.17^\circ$ , and the Regime II/III change occurs at position 12. There are six viewing positions for each Regime. For the dark surface case, agreement is better than 1% everywhere, with a high bias of around 0.5% for VLIDORT-QS. Once again, the bias is slightly larger for the albedo 0.25 case (around 0.7%).

For a third example km in Figure 3.4, we keep the camera at 16.5, but the 40-layer Rayleigh atmosphere now includes a sulfate aerosol layer of 4.5 km geometrical thickness in the same Rayleigh

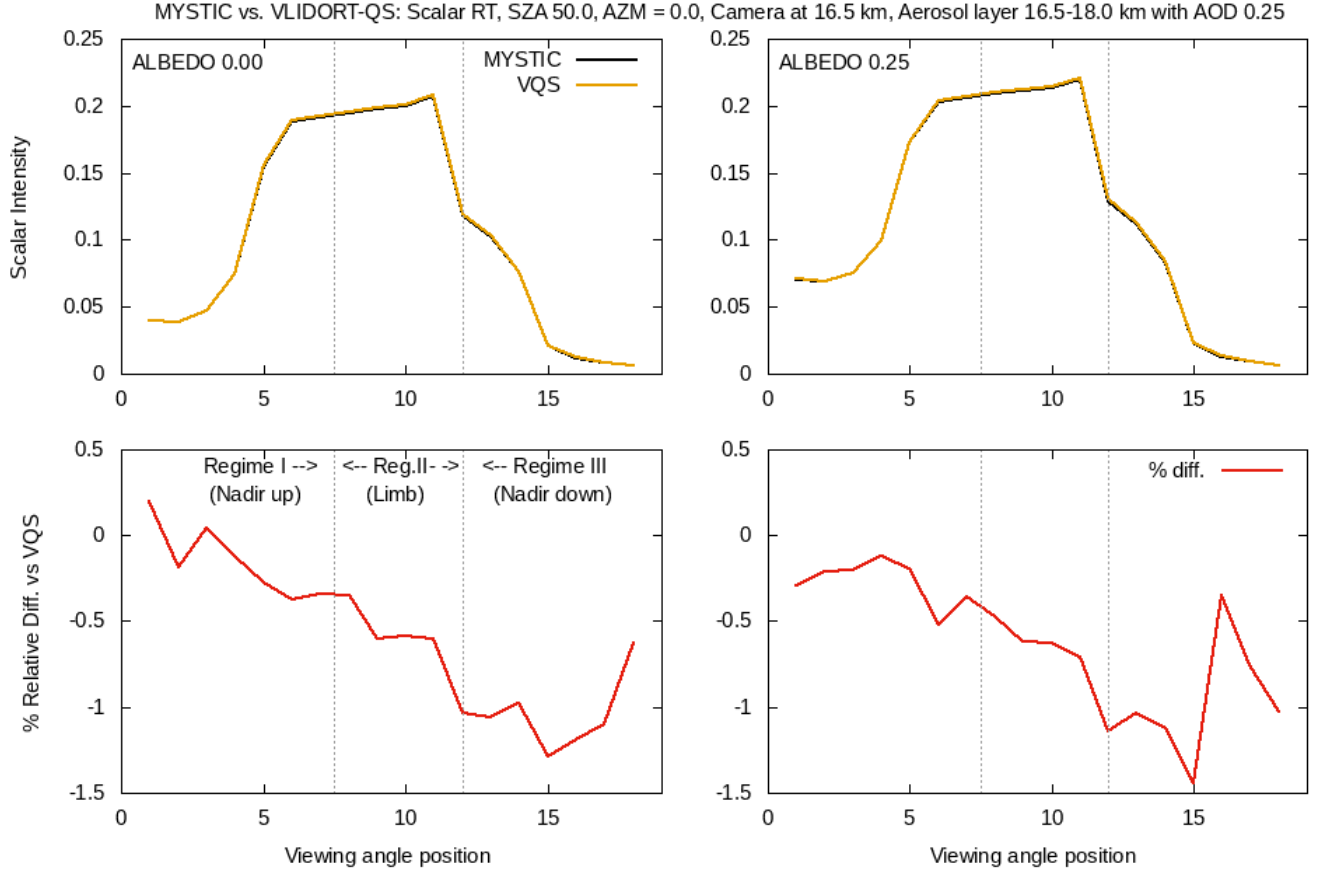


**Figure 3.4.** Comparisons against MYSTIC MC model, scalar RT, again with the camera at 16.5 km, but now including an aerosol layer of optical thickness 0.25 between 12.0 km and 16.5 km, and for SZA = 50° in the principal plane. LZA positions are the same as those in the previous figure. (Top) VLIDORT-QS and MYSTIC results for albedo = 0.0 and 0.25; (lower panels) relative differences.

atmosphere. The aerosol layer occupies a position just below the camera location where an aerosol optical thickness value of 0.25 was used. Scattering properties for a sulfate aerosol at 371nm were obtained from the Optical Properties of Aerosol and Clouds (OPAC) database [32] included in LibRadtran [7]. We use eight polar half-space discrete ordinates in the VLIDORT-QS MS solution, which also includes the delta-M scaling ansatz for dealing with forward scattering enhancement. MYSTIC calculations were done with 1 Million photons. There is again a small bias – VLIDORT-QS tends to overestimate by up to 1.5%.

## 4. Application – Smoke-Plume Scenario

In this section, we demonstrate the power and flexibility of VLIDORT-QS for a familiar application - the biomass-burning smoke-plume scenario. We simulate the radiation field detected by a camera positioned on an aircraft that can fly over, through and below a tropospheric smoke plume. We take the camera to have a complete view angle capability from the zenith through limb views all the way to the nadir. The plume is modeled with a Gaussian aerosol loading profile, characterized by three parameters: the total aerosol optical depth (AOD) at a reference wavelength, the peak height for the plume, and the Gaussian half-width. UV trace gas absorption by HCHO, NO<sub>2</sub> and O<sub>3</sub> is also considered, with Rayleigh scattering

in all layers. In the plume, aerosol scattering and extinction properties are modeled with Mie code calculations based on mixtures of black and brown carbon. Of particular interest here is the retrieval of aerosol and trace gas profiles in the troposphere, and we will use the linearization facility of the VLIDORT-QS model to examine weighting function outputs from the model.

Specifically, we consider a Gaussian plume situated between 1.0 and 4.0 km, having a peak concentration height at 2.5 km, a half width value of 0.4 km, and a total AOD of 1.91 at 354 nm. The plume is partitioned into 30 sub-layers at vertical resolution 0.1 km. Atmospheric conditions (pressure, temperature and height) are taken from the US Standard mid-latitude summer atmosphere, interpolated as necessary to the fine-layer gridding inside the plume, and with a vertical resolution of 0.25 km for layering in the free troposphere up to 12 km above the plume. Trace gas volume mixing ratio profiles are taken from the Deriving Information on Surface conditions from Column and Vertically Resolved Observations Relevant to Air Quality (DISCOVER-AQ) data (see for example [33]), and corresponding absorber cross-sections come from a compilation of laboratory data assembled for the Tropospheric Emissions: Monitoring Pollution (TEMPO) mission [34]. Rayleigh scattering properties are based on the formulation in [35].

We first look at the radiation field at three camera positions (1.0, 2.5 and 4.0 km) at the bottom, peak height and top of the plume. The SZA is  $45^\circ$  at each camera position, with relative azimuth set to  $90^\circ$ , and we allow the LZA to take values over the range  $[0^\circ, 180^\circ]$  (nadir to zenith).

For the camera at 1.0 km (bottom of the plume), the Regime I viewing angles range from  $0^\circ$  to  $88.98^\circ$ ; the LOS starts at the surface. For Regime II limb views, the LOS passes completely through the plume and then traverses part of the lowest 0–1 km of the atmosphere before ending up at the camera.

For the camera at 4 km (top of the plume), Regime I LZAs run from  $0^\circ$  to  $87.97^\circ$ , with all LOS paths starting at the surface and passing through the plume. In this case, the Regime II limb views divide naturally into two types: Regime IIa, in which the LOS path passes downwards completely through the plume, then through a tangent height in the lower atmosphere below the plume, and finally passing upward through the plume again to the Camera (LZA range  $87.97^\circ$  to  $88.24^\circ$ ); and Regime IIb where the LOS passes through a tangent height that is *inside* the plume (LZA range  $88.24^\circ$  to  $90^\circ$ ). With the camera at 4 km, Regime III LOS paths pass only through the clear atmosphere above the plume, and Rayleigh scattering is dominant.

For the camera at 2.5 km (peak height), Regime I VZAs run from  $0^\circ$  to  $88.395^\circ$ , and there are again two parts to the Regime II limb views – those that pass completely through the plume and continue through part of the clear atmosphere below the plume before a re-entry and passage through part of the plume to the mid-point position (IIa), and those limb views for which the tangent height is inside the plume. For Regime III views, part of each downwelling LOS path will be through the plume.

Calculations were carried out for scalar (no polarization) scenarios with VLIDORT-QS, using 12 discrete ordinates in the polar half space for the MS contributions, and 20 fine-resolution divisions for the segment quadrature.



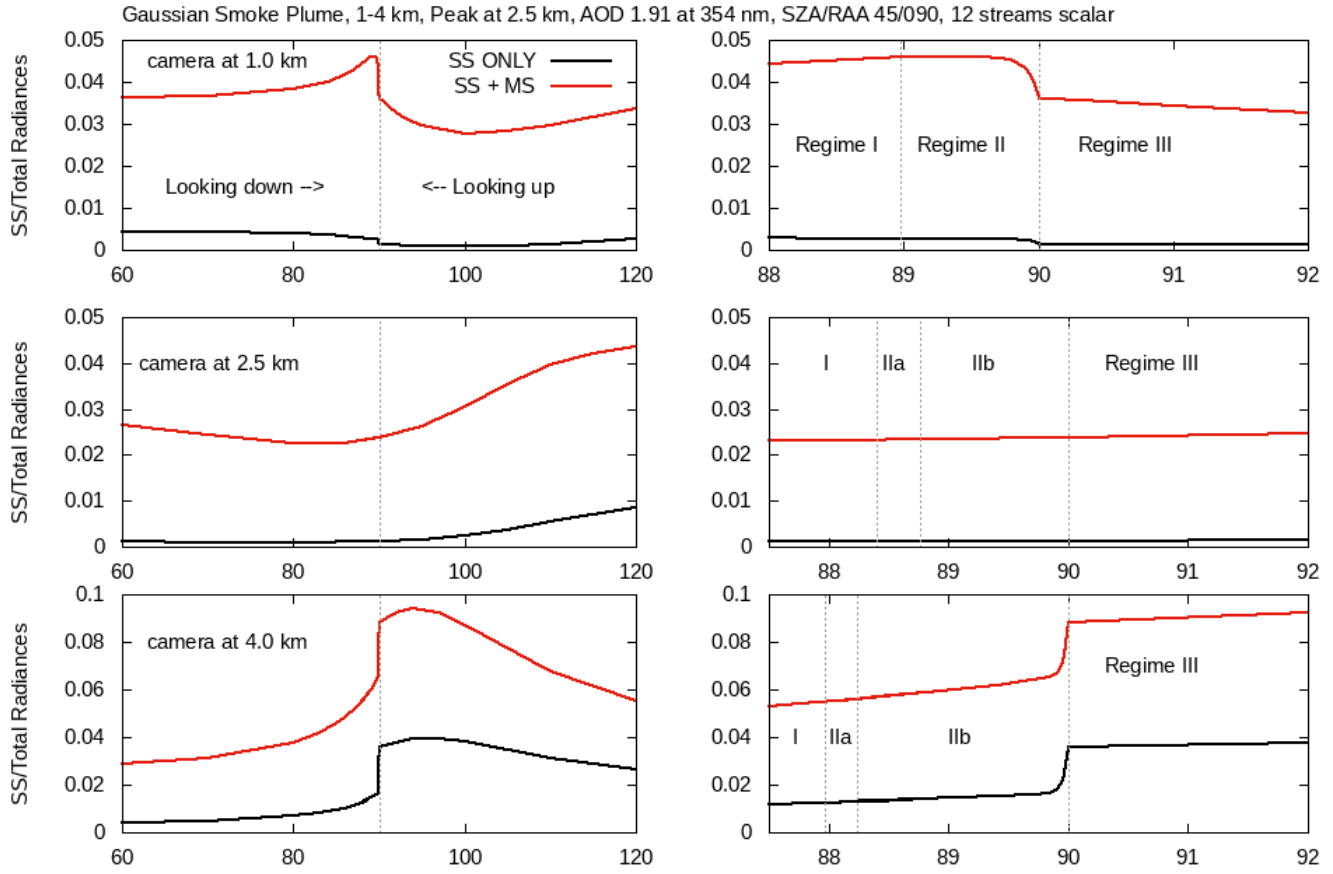


**Figure 4.1.** SS and total (SS+MS) radiances at three camera positions in the plume, plotted for LZAs running from 60° to 120° (left column plots), with a magnified view for LZA range 87.5° to 92° (right column). See text for an explanation of the Regime viewing conditions.

At the bottom of the plume (top row in Figure 4.1), MS dominates, with the largest radiances for views looking down into the Rayleigh atmosphere below the plume; there is a sudden drop in radiance once the LOS paths traverse the aerosol plume above the camera. At the peak height (middle row), the camera is fully immersed in the plume and there are no sudden changes in radiance values from upwelling to downwelling; not surprisingly the MS contributions tend to dominate in what is a fairly optically thick plume medium. At the plume upper boundary, there is a clear jump going from upwelling paths through the plume, to downwelling paths with only a passage through the free troposphere above the plume.

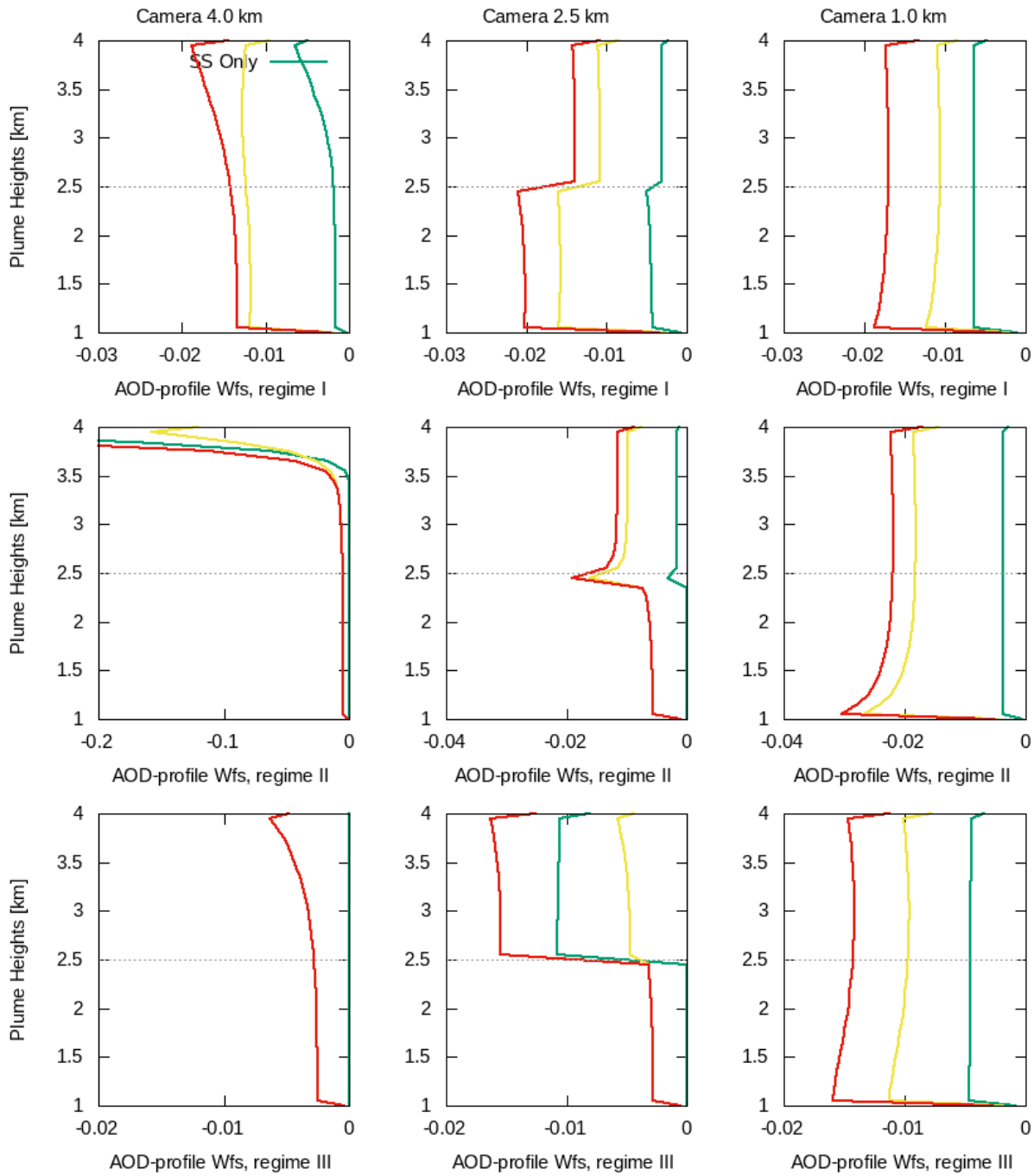


**Figure 4.2.** SS (green), MS (yellow) and combined (red) aerosol optical depth profile Jacobians at three camera positions as indicated (4.0 km at the top of the plume, 2.5 km in at the plume peak height, and 1.0 km at the lower boundary of the plume), plotted for a LZA of  $35^\circ$  (Regime I, upper row),  $89^\circ$  (Regime II, middle row), and  $125^\circ$  (Regime III, bottom row). The plume is spread between 1.0 and 4.0 km with vertical resolution 0.1 km (40 sub-layers), with total plume optical thickness 1.908 at 354 nm. 8 half-space polar discrete ordinates were used in the MS calculations.

Lastly, we examine aerosol profile Jacobians for the same plume scenario, with the camera again set at the three positions as noted above, and with the same solar and azimuth angles, but this time with three

LOS settings corresponding to a Regime I nadir-upwelling view ( $LZA = 35^\circ$ ), a Regime II limb view ( $LZA = 89^\circ$ ), and a Regime III zenith-downwelling view ( $LZA = 125^\circ$ ). There are 30 Jacobians to calculate, one for each of the fine-layer sub-divisions inside the plume; these Jacobians are defined as  $K_n = \partial I / \partial \tau_n$ , where  $\{\tau_n\}, n = 1, \dots, 30$  are the fine-layer aerosol optical thickness values in the plume, and  $I$  is the radiance at a given camera position. These Jacobians are displayed in Figure 4.2 with the SS values (green) compared against the MS contributions (yellow), and the combined (SS+MS) Jacobians (red).

## 5. Concluding Remarks

In this paper, we report on a new quasi-spherical polarized RT model, VLIDORT-QS, developed for nadir- and limb-viewing geometrical configurations in planetary atmospheres. The SS calculation is always performed for a fully-spherical atmosphere. MS solutions to the RTE are still calculated for plane-parallel media using the VLIDORT discrete ordinates model in the pseudo-spherical approximation, but now the source-function integration of all MS fields is done in spherical geometry. The VLIDORT-QS model is fully linearized with respect to atmospheric profile parameters, and will deliver Stokes vectors and associated profile Jacobians at any level in the atmosphere, for upwelling or downwelling nadir-view scenarios and for any limb-view geometry. The model is validated in two different ways: first against the VLIDORT model for typical upwelling and downwelling nadir- and zenith-view scenarios with and without VLIDORT's new sphericity correction procedure, and secondly against a spherical Monte Carlo RT model for two atmospheric scenarios designed to test all the viewing possibilities in VLIDORT-QS. We also demonstrate the use of VLIDORT-QS for a biomass-burning plume application.

In a second paper, we will use VLIDORT-QS to carry out an investigation of ice and water-cloud retrievals in the near infra-red (900–1726 nm), from limb- and nadir-view measurements taken by a spectrometer on board NASA's high-altitude Global Hawk aircraft during a series of missions under the aegis of the ATTREX project. Retrievals will focus on long-path ice-cloud and water-cloud extinction and absorption, and will include trace gas absorptions from three trace species ( $H_2O$ ,  $CO_2$ , and  $O_2$ ).

**Acknowledgments.** This work was supported in part under NASA Award NNX14AP81G (Investigation of TTL cirrus cloud properties using Near-IR absorption spectroscopy during ATTREX), and in part through NASA Award 80NSSC21K1447 (Advancing UV/Vis remote sensing of biomass burning plumes: Brown carbon, actinic flux, and trace gas retrievals). A portion of this research was carried out at the Jet Propulsion Laboratory, California Institute of Technology, under a contract with the National Aeronautics and Space Administration (80NM0018D0004).

## 6. References

- [1] Adams CN, Kattawar GW. Radiative transfer in spherical shell atmospheres. I. Rayleigh scattering. *Icarus* 1978;35:139-151.
- [2] Postylyakov OV. Linearized vector radiative transfer model MCC++ for a spherical atmosphere, *J Quant Spect Rad Trans* 2004;88:297-317.
- [3] Deutschmann T, Beirle S, Fries U, Grzegorski M, Kern C, Kritten L, Platt U, Prados-Roman C, Pukite J, Wagner T, Werner B, Pfeilsticker K. The Monte Carlo atmospheric radiative transfer model McArtim: Introduction and validation of Jacobians and 3D features. *J Quant Spect Rad Tran* 2011; 112:1119-1137.

- [4] Emde C, Buras-Schnell R, Kylling A, Mayer B, Gasteiger J, Hamann U, Kylling J, Richter B, Pause C, Dowling T, and Bugliaro L. The libRadtran software package for radiative transfer calculations (version 2.0.1). *Geosci Model Dev* 2016;9:1647-1672.
- [5] Mayer B. Radiative transfer in the cloudy atmosphere. *European Physical Journal Conferences* 2009;1:75-99.
- [6] Dahlback A, Stamnes K. A new spherical model for computing the radiation field available for photolysis and heating at twilight. *Planet Space Sci* 1991;39:671-683.
- [7] Mayer B, Kylling A. Technical note: The libRadtran software package for radiative transfer calculations - description and examples of use. *Atmos. Chem. Phys* 2005;5:1855-1877.
- [8] Rozanov V, Rozanov A, Kokhanovsky A, Burrows J. Radiative transfer through terrestrial atmosphere and ocean: Software package SCIATRAN. *J Quant Spect Rad Trans* 2014;133:13-71.
- [9] Doicu A, Trautmann T. Discrete-ordinate method with matrix exponential for a pseudospherical atmosphere: Scalar case. *J Quant Spect Rad Trans* 2009a;110:146–158.
- [10] Spurr R. LIDORT and VLIDORT: Linearized pseudo-spherical scalar and vector discrete ordinate radiative transfer models for use in remote sensing retrieval problems. In: Kokhanovsky A, editor. *Light Scattering Reviews: Vol 3*: Springer; 2008.
- [11] Spurr R, Christi M. The LIDORT and VLIDORT linearized scalar and vector discrete ordinate radiative transfer models: updates in the last 10 years. In: Kokhanovsky A, editor. *Light Scattering Reviews: Vol 12*: Springer; 2019, p. 1-62.
- [12] Herman BM, Ben-David A, Thome JK. Numerical technique for solving the radiative transfer equation for spherical shell atmosphere. *Applied Optics* 1994;33:1760-1770.
- [13] Loughman R, Flittner D, Nyaku E, Bhartia PK. Gauss–Seidel limb scattering (GSLs) radiative transfer model development in support of the Ozone Mapping and Profiler Suite (OMPS) limb profiler mission. *Atmos Chem Phys* 2015; 15:3007-3020.
- [14] Doicu A, Trautmann T. Picard iteration methods for a spherical atmosphere. *J Quant Spect Rad Trans* 2009b;110:1851–1863.
- [15] Rozanov A, Rozanov V, Burrows JP. A numerical radiative transfer model for a spherical planetary atmosphere: combined differential-integral approach involving the Picard iterative approximation. *J Quant Spect Rad Trans* 2001;69:491-512.
- [16] Walter HH, Landgraf J, Spada F, Doicu A. Linearization of a radiative transfer model in spherical geometry. *J Geophys Res* 2006;111:D24304.
- [17] Korkin S, Yang E-S, Spurr R, Emde C, Krotkov N, Vasilkov A, Haffner D, Mok J, Lyapustin A. Revised and extended benchmark results for Rayleigh scattering of sunlight in spherical atmospheres. *J Quant Spect Rad Trans* 2020;254:107181.
- [18] Spurr RJD. VLIDORT: A linearized pseudo-spherical vector discrete ordinate radiative transfer code for forward model and retrieval studies in multilayer multiple scattering media. *J Quant Spect Rad Trans* 2006;102:316-342.
- [19] Caudill TR, Flittner DE, Herman BM, Torres O, McPeters RD. Evaluation of the pseudo-spherical approximation for backscattered ultraviolet radiances and ozone retrieval. *J Geophys Res* 1997;102:3881-3890.

- [20] Rozanov AV, Rozanov VV, Burrows JP. Combined differential-integral approach for the radiation field computation in spherical shell atmosphere: Non-limb geometry. *J Geophys Res* 2000;105:22937-22942.
- [21] Spurr R. LIDORT V2PLUS: a comprehensive radiative transfer package for UV/VIS/NIR nadir remote sensing. *Proc SPIE* 2004;5235:89-100.
- [22] ESA, Cassini-Huygens mission objectives. 2005. <https://sci.esa.int/web/cassini-huygens/2085-objectives/>.
- [23] Jensen EJ, Pfister L, Jordan DE, Bui TV, Ueyama R, Singh HB, Thornberry TD, Rollins AW, Gao R-S, Fahey DW, Rosenlof KH, Elkins JW, Diskin GS, DiGangi JP, Lawson RP, Woods S, Atlas EL, Navarro-Rodriguez MA, Wofsy SC, Pittman J, Bardeen CG, Toon OB, Kindel BC, Newman PA, McGill MJ, Hlavka DL, Lait LR, Schoeberl MR, Bergman JW, Selkirk HB, Alexander MJ, Kim J-E, Lim BH, Stutz J, Pfeilsticker K. The NASA Airborne Tropical Tropopause Experiment: High-Altitude Aircraft Measurements in the Tropical Western Pacific. *Bull Am Meteor Soc* 2017;98:129–143. doi:10.1175/BAMS-D-14-00263.1.
- [24] Spurr R. Simultaneous radiative transfer derivation of intensities and weighting functions in a general pseudo-spherical treatment. *J Quant Spect Rad Trans* 2002;75:129-175.
- [25] Nakajima T, Tanaka M. Algorithms for radiative intensity calculations in moderately thick atmospheres using a truncation approximation. *J Quant Spect Rad Trans* 1988;40:51-69.
- [26] Emde C, Mayer B. Simulation of solar radiation during a total solar eclipse: a challenge for radiative transfer. *Atmos Chem Phys* 2007;7:2259-2270.
- [27] Ockenfuss P, Emde C, Mayer B, Bernhard G. Accurate 3D radiative transfer simulation of spectral solar irradiance during the total solar eclipse of August 21, 2017. *Atmos Chem Phys* 2020; 20:1961-1976.
- [28] Buras R, Mayer B: Efficient unbiased variance reduction techniques for Monte Carlo simulations of radiative transfer in cloudy atmospheres: The solution. *J Quant Spect Rad Trans* 2011;112:434-447.
- [29] Korkin S, Yang E-S, Spurr R, Emde C, Zhai P, Krotkov N, Vasilkov A, Haffner D, Mok J, Lyapustin A. Numerical results for polarized light scattering in a spherical atmosphere. *J Quant Spect Rad Trans* 2022. <https://doi.org/10.1016/j.jqsrt.2022.108194>.
- [30] Anderson GP, Clough SA, Kneizys FX, Chetwynd JH, Shettle EP, AFGL (Air Force Geophysical Laboratory) atmospheric constituent profiles (0-120km), Environmental research papers, Rep. # AFGL-TR-86-0110, Air Force Geophysics Lab., Hanscom AFB, MA, USA, 1986.
- [31] van Oss, R F, Spurr, R: Fast and accurate 4-stream linearized discrete ordinate radiative transfer models for ozone profile retrieval, *J Quant Spect Rad Trans* 2002; 75: 177-220.
- [32] Hess M, Koepke P, Shult I. Optical Properties of Aerosol and Clouds: The Software Package OPAC. *Bull Am Meteor Soc* 1998;79:831-844.
- [33] Goldberg D, Loughner C, Tzortziou M, Stehr J, Pickering K, Marufu L, Dickerson R. Higher surface ozone concentrations over the Chesapeake bay than over the adjacent land: Observations and models from the DISCOVER-AQ and CBODAQ campaigns. *Atmos Environ* 2014;84:9-19.

- [34] Zoogman P, et. al. Tropospheric Emissions: Monitoring of Pollution (TEMPO). J Quant Spect Rad Trans 2017;186:17-39.
- [35] Bodhaine B, Wood N, Dutton E, Slusser J. On Rayleigh optical depth calculations. J Atmos Ocean Tech 1999;20:1854-1861.